

# Title

## Differential requirements of cyclase associated protein (CAP) for actin turnover during the lytic cycle of *Toxoplasma gondii*

Alex Hunt<sup>1</sup>, Jeanette Wagener<sup>1</sup>, Robyn Kent<sup>2</sup>, Romain Carmeille<sup>3</sup>, Matt Russell<sup>4</sup>, Christopher Peddie<sup>4</sup>, Lucy Collinson<sup>4</sup>, Aoife Heaslip<sup>3</sup>, Gary E. Ward<sup>2</sup> & Moritz Treeck<sup>1\*</sup>

<sup>1</sup> Signalling in Apicomplexan Parasites Laboratory, The Francis Crick Institute, United Kingdom

<sup>2</sup> Department of Microbiology and Molecular Genetics, University of Vermont Larner College of Medicine, Burlington, Vermont, United States

<sup>3</sup> Department of Molecular and Cell Biology, University of Connecticut, Connecticut, United States

<sup>4</sup> Electron Microscopy Science Technology Platform, The Francis Crick Institute, United Kingdom

\*For correspondence: [moritz.treeck@crick.ac.uk](mailto:moritz.treeck@crick.ac.uk)

## Abstract

*Toxoplasma gondii* contains a limited subset of actin binding proteins. Here we show that ablation of the putative actin regulator cyclase-associated protein (TgCAP) leads to significant defects in some but not all actin dependent processes, including a defect in cell-cell communication, but surprisingly not synchronicity of division. Two CAP isoforms originate from alternative translational start sites and are beneficial for parasite fitness while a single isoform is sufficient for virulence in mice. Examination of the mutant parasites by 3D electron microscopy reveals that loss of CAP results in a defect to form a normal residual body, but all parasites remain connected within the vacuole. This dissociates synchronicity of division and parasite rosetting and reveals that establishment and maintenance of the residual body may be more complex than previously thought. These results highlight the different spatial requirements for actin turnover in *Toxoplasma*, controlled by a reduced subset of actin binding proteins.

## Introduction

*Toxoplasma gondii* is an obligate intracellular parasite, belonging to the Apicomplexa phylum. The Apicomplexa, which also include *Plasmodium* and *Cryptosporidium* species, pose a significant global public health burden. *Toxoplasma*, specifically, is one of the most prevalent human pathogens, chronically infecting ~30% of the world's population (Swapna & Parkinson, 2017). While most infections are asymptomatic, in congenitally infected and immunocompromised patients, disease outcomes are often severe and potentially fatal (Halonen & Weiss, 2013). During acute infection of the host, the asexual tachyzoite stage of *Toxoplasma gondii* undergoes cycles of active invasion, replication and egress from host cells. This lytic cycle leads to rapid proliferation and dissemination of the parasite throughout the host (Black & Boothroyd, 2000). To facilitate these processes, *Toxoplasma* utilises a unique form of locomotion, called gliding motility, which relies on actin and an unconventional myosin motor (Frénal, Dubremetz, et al., 2017). This motor allows the parasite to actively invade host cells, where it forms a protective parasitophorous vacuole (PV). PV structural integrity and stability is sustained through the parasite's release of dense granule proteins from secretory vesicles (Heaslip et al., 2016). Additionally, several dense granule proteins are transported into the host cell where they co-opt or interfere with host cell functions (Hakimi et al., 2017). Within the PV, *Toxoplasma* begins a unique form of cell division called endodyogeny (Sheffield & Melton, 1968). Here, two daughter cells are synchronously assembled within the mother cell before daughter cell budding (Delbac et al., 2001). This initiates at the apical pole of the mother cell and once complete, the daughter cells bud from the mother cell but remain attached at their basal pole to the residual body: a membranous compartment containing maternal remnants of organelles and cytoskeletal elements (Muñiz-Hernández et al., 2011). During cell division, organelles such as mitochondria and the apicoplast, a unique and essential organelle

which contributes to isoprenoid synthesis (Vaishnava & Striepen, 2006), also divide and are distributed between the two daughter parasites. Following multiple rounds of cell division, parasites organise into a rosette-like pattern around the residual body. Formation of the characteristic rosette pattern requires actin, several myosins, and other actin-binding proteins (Frénal, Jacot, et al., 2017; Haase et al., 2015; Jacot et al., 2013; Periz et al., 2017; Tosetti et al., 2019). It has been hypothesised that the inter-parasite connections via the residual body are not only important for parasite organisation, but also play a key role in cell-cell communication. Such communication was measured by the transfer of reporter proteins between parasites and is believed to ensure the synchronous division of parasites within a vacuole (Frénal, Jacot, et al., 2017). The parasites continue to replicate until host cell lysis and parasite egress. Following egress, parasites migrate to and invade new host cells and the lytic cycle repeats, leading to tissue destruction (Black & Boothroyd, 2000). Actin plays an essential role in the parasite's lytic cycle through function of the actin cytoskeleton and actomyosin motor complex. Despite this crucial role in apicomplexan biology, there has been difficulty visualising actin filaments in apicomplexan species (Bannister & Mitchell, 1995; Sahoo et al., 2006; Shaw & Tilney, 1999) and it has been suggested that as much as 98% of parasite actin is monomeric (G-actin) and not incorporated into filaments (F-actin) (Dobrowolski et al., 1997). This, along with structural differences found in actin of Apicomplexa (Pospich et al., 2017), led to the hypothesis that *Toxoplasma* F-actin has reduced stability, forming abnormally short filaments that are rapidly recycled to maintain essential cellular function (Pospich et al., 2017; Skillman et al., 2011). However, recent development of the actin-chromobody has allowed for the visualisation of long F-actin structures both in the parasite and extensive networks within the PV (Periz et al., 2017). Taken together, along with biochemical evidence, apicomplexan actin appears to be different to actin from other organisms (Frénal, Dubremetz, et al., 2017).

Actin turnover is regulated by actin binding proteins, of which *Toxoplasma* possesses a reduced repertoire, including ADF/cofilin, profilin, coronin and cyclase-associated protein (CAP) (Baum et al., 2006). Functional studies have shown ADF/cofilin and profilin to be essential for *Toxoplasma* progression through the lytic cycle, while coronin depletion had a modest impact on parasite invasion and egress (Mehta & Sibley, 2011; Plattner et al., 2008; Salamun et al., 2014). Apart from its localisation, the function of CAP in *Toxoplasma* has not been investigated. In the majority of eukaryotes, CAP is a highly conserved multidomain protein that regulates actin filament dynamics via two distinct mechanisms (Ono, 2013). CAP can bind and sequester G-actin using its CAP and X-linked retinitis pigmentosa 2 protein (CARP) domain and can regulate actin filament disassembly by promoting ADF/cofilin mediated severing using its helical folded domain (HFD). Through regulation of actin dynamics, by interacting with actin and other actin binding proteins, it has been shown that mouse CAP1 plays important roles in cell morphology, migration and endocytosis (Bertling et al., 2004). However, species belonging to the Apicomplexa phylum possess a truncated form of CAP, retaining only the conserved C-terminal G-actin-binding CARP domain (Hliscs et al., 2010). This conserved  $\beta$ -sheet domain has been shown to interact directly with monomeric actin, providing either sequestration or nucleotide exchange of G-actin in a concentration-dependent manner (Hliscs et al., 2010; Makkonen et al., 2013; Mattila et al., 2004). As such, apicomplexan CAP is hypothesised to regulate actin turnover solely through interaction with monomeric actin. Biochemical analysis of *Cryptosporidium parvum* CAP identified the formation of a dimer and G-actin sequestering activity, while *Plasmodium falciparum* CAP was shown to facilitate nucleotide exchange, loading ADP-actin monomers with ATP (Hliscs et al., 2010; Makkonen et al., 2013). A *Plasmodium berghei* CAP KO demonstrated that while PbCAP is dispensable for asexual blood stages *in vivo*, there is a complete defect in oocyst development in the insect vector which was overcome through complementation with *C. parvum* CAP (Hliscs et al., 2010). A PbCAP overexpression study revealed no defect in ookinete motility or oocyst development, however sporozoites displayed impaired gliding motility, invasion and salivary gland colonisation (Sato et al., 2016). Taken together, these results suggest that apicomplexan CAP may function as a dimer with the ability to interact with G-actin monomers to sequester them and/or facilitate their nucleotide exchange. While CAP has yet to be functionally

characterised in *Toxoplasma*, Lorestani *et al* reported that CAP localises to the apex of intracellular parasites, a hub for events leading to egress and motility (Graindorge *et al.*, 2016; Lorestani *et al.*, 2012; Tosetti *et al.*, 2019). Intriguingly, following host cell lysis, relocalisation of CAP to the parasite cytosol was observed (Lorestani *et al.*, 2012). Furthermore, we have previously identified differential phosphorylation of TgCAP in parasites with a delayed egress phenotype (Treeck *et al.*, 2014). The correlation between TgCAP redistribution and phosphorylation, following host cell lysis, hints at a potential role for TgCAP in actin regulation during rapid egress. Taken together, these results prompted us to characterise the role of TgCAP in *Toxoplasma* biology.

Here we show that TgCAP is produced in two distinctly localised isoforms through alternative translation initiation: a membrane bound isoform, localised to the apical tip (longCAP) and a cytosolically dispersed isoform (shortCAP). Conditional knockout of TgCAP, using a second generation DiCre strain, identified an important function of TgCAP in some, but not all, actin-dependent processes. Invasion, egress, motility, correct daughter cell orientation and dense granule trafficking were all perturbed in CAP depleted parasites, while apicoplast inheritance was not. This suggests different spatial requirements for CAP in actin turnover within the cell. Furthermore, the characteristic rosette organisation of parasites in the vacuole was completely lost, but synchronicity of division was unaffected. Strikingly, while we observe rapid protein transfer only between two adjacent cells in a vacuole, all parasites remain connected through a decentralised residual body, potentially explaining why synchrony of division is unaffected. In the mouse *in vivo* infection model, CAP-depleted type I RH parasites display normal lethality, while CAP depletion renders type II Pru parasites avirulent, with markedly reduced cyst formation. Furthermore, the cytoplasmic isoform of TgCAP was sufficient for the infection of mice and the formation of latent stages in the brain, indicating that the apically localised CAP isoform provides only a small fitness benefit under the conditions tested here.

## Results

### **TgCAP contains two translational start sites which results in the production of two differentially localised protein isoforms.**

TgCAP was previously shown to localise to the apex of intracellular parasites and rapidly redistribute to the cytoplasm of extracellular parasites following host cell lysis (Lorestani *et al.*, 2012). This suggested that TgCAP localisation may be influenced by post-translational modifications that enable CAP to regulate actin dynamics at different locations in the cell. TgCAP, and CAP from *Neospora* and *Hammondia* species contain a unique predicted N-terminal extension that is not present in other Apicomplexa, such as *Plasmodium* (Fig 1A). The extension contains two predicted palmitoylation sites and CAP was identified in an analysis of palmitoylated proteins in *Toxoplasma gondii* (Foe *et al.*, 2015). Furthermore, two phosphorylation sites in the N-terminus of TgCAP are substantially phosphorylated upon ionophore-induced egress (Treeck *et al.*, 2014). These phosphorylation events are dependent on the calcium-dependent kinase 3 (TgCDPK3) (Treeck *et al.*, 2014), which has been shown to be important in mediating rapid exit from the host cell and is localised to the plasma membrane (Black *et al.*, 2000; Garrison *et al.*, 2012; Lourido *et al.*, 2012; McCoy *et al.*, 2012). Collectively, these observations allow for the possibility that re-localisation of CAP is important for egress and is mediated by dynamic post-translational modifications. To visualise TgCAP we expressed it as a GFP fusion. TgCAP-GFP localises to the apex of the parasite, as previously shown, but also to the cytoplasm of intracellular tachyzoites (Fig. 1B). We additionally demonstrated this dual localisation of TgCAP by C-terminally tagging the endogenous TgCAP locus with a HA epitope tag (Supplementary Fig. 1). To rule out any mislocalisation of the protein as a result of tagging, we expressed recombinant TgCAP, spanning residues 37 to 203, and generated antibodies against TgCAP which confirmed the dual localisation (Fig 1C). Western blot analysis of parasite lysates revealed the presence of two bands close to the expected size of TgCAP, which are expressed at a constant level, relative to the *Toxoplasma* loading control, across the first 24 hours following host cell invasion (Fig. 1D). The dual localisation of CAP could be due to the expression of two isoforms from a single

gene, through use of alternate translational start sites, as previously observed for protein kinase G (Brown et al., 2017). Indeed, sequence comparison of TgCAP to PfCAP reveals a second in-frame methionine at position 37 in *Toxoplasma* that aligns with the PfCAP start methionine (Fig. 1A). Two additional methionine residues, M71 and M161, are present in the CAP primary sequence. However, these are unlikely used as translational start sites as their products would lead to a truncated and potentially inactive CARP domain.

Translational start sites in eukaryotic mRNAs are preceded by a translation initiation sequence (Kozak, 1987a, 1987b). Consensus translation initiation sequences have been determined for many different organisms and are known as the Kozak sequence (Nakagawa et al., 2008). In *Toxoplasma*, the Kozak sequence was elucidated by identifying nucleotides commonly found in highly abundant proteins, such as SAG1 (Seeber, 1997). This Kozak sequence contains an adenine at the -3 position, relative to the start ATG, and was identified as the most important factor in ribosomal recognition of the start ATG (Seeber, 1997). Absence of an adenine can result in ribosome “leaky scanning” and translation from an internal ATG. We therefore analysed the translation initiation sequence around CAP’s first (M1) and second (M37) putative translational start sites. The M1 translation initiation sequence conforms less with the *Toxoplasma* Kozak sequence than the sequence preceding M37; as the former is lacking an adenine at the -3 position (Fig. 1E). This suggested that alternative translation could lead to the generation of two CAP isoforms: longCAP, which is translated from the first start ATG, and shortCAP, which is translated from the second start ATG. To test this, we generated parasite strains that expressed either the WT sequence or variants where either the first (M1), or the second methionine (M37) of TgCAP was mutated to leucine, precluding their use as translational start sites (Fig. 1F). We used the endogenous promoter (i.e. 969 bp upstream of the first start ATG) and introduced the C-terminal HA-tagged TgCAP variants into the *UPRT* locus of the RH DiCre $\Delta ku80\Delta hvgprt$  parasite strain. To determine whether longCAP and shortCAP show differential localisation, as predicted by the presence of putative palmitoylation sites in longCAP, we analysed their subcellular localisation using the HA-tag. While WT CAP parasites showed the expected dual localisation, mutants expressing shortCAP showed exclusively cytoplasmic staining while those expressing longCAP showed predominantly apical staining, with some further signal throughout the parasite (Fig. 1G). As longCAP contains two putative palmitoylation sites not present in the shortCAP sequence, we next evaluated whether palmitoylation was important for the apical localisation of the long CAP isoform. We mutated the two cysteines in the N-terminus to alanine residues (CAP\_C6,8A). CAP\_C6,8A appeared cytosolic with no detectable accumulation of CAP at the apical end of the parasites (Fig. 1G). Western blot analysis of the HA-tagged TgCAP variants confirmed that WT CAP is identified as two distinct protein bands, which correlate with the predicted size for longCAP and shortCAP (23.9 and 20 kDa). Parasites expressing shortCAP displayed only the lower molecular weight band, while longCAP-expressing parasites only showed the higher molecular weight band. We observed that the protein levels of longCAP appear reduced compared to its isoform in parasites expressing WT CAP, whereas the shortCAP isoform shows an increase (Fig. 1H). As expected, despite CAP\_C6,8A not being detected at the apical end of the parasite, both isoforms were detected by Western blot at levels comparable to parasites expressing WT CAP. Collectively, these results show that in *Toxoplasma*, and potentially closely related coccidian parasites of *Hammondia* and *Neospora*, CAP is produced as two differentially localised isoforms using alternative translational start sites and the apical localisation of the long isoform is likely palmitoylation dependent.

# **Generation of a more stable RH DiCre $\Delta ku80$ cell line**

While attempting to generate a conditional knock out (cKO) of CAP using the DiCre strategy, we observed a frequent loss of one of the DiCre subunits, resulting in dysfunctional floxed CAP parasite strains that lacked the ability to excise CAP. This is possibly because both DiCre subunits are driven by identical 5’ and 3’ UTRs, allowing for potential recombination in the  $\Delta ku80$  parental line, which possesses an increased efficiency of homologous recombination (Fox et al., 2009; Huynh & Carruthers, 2009). To prevent loss of DiCre subunits, we generated



a new DiCre construct, DiCre\_T2A, that expresses the two DiCre subunits from a single promoter using T2A skip peptides (Kim et al., 2011). To further minimise the potential for loss of DiCre, we placed a chloramphenicol acetyltransferase (CAT) selectable marker between the two subunits (Fig. 2A). This would lead to the production of the two separate Cre subunits and the CAT selectable marker. We inserted this construct, into the modified *KU80* locus of the RH  $\Delta ku80\Delta hxcgprt$  strain (Huynh & Carruthers, 2009) using CRISPR/Cas9. To test whether expression of the DiCre subunits in the resulting line, RH DiCre\_T2A  $\Delta ku80\Delta hxcgprt$ , is stable over time, we integrated the loxP-KillerRed-loxP-YFP reporter construct used in Andenmatten et al., into the *UPRT* locus (Andenmatten et al., 2013). As expected, non-treated parasites express KillerRed which, upon RAP treatment, is excised and leads to expression of YFP (Fig. 2B). As extracellular stress can lead to increased loss of DiCre activity in the original DiCre line (M. Meissner, personal communication, 02.2019), we subjected the new DiCre parasite line (RH DiCre\_T2A  $\Delta ku80\Delta hxcgprt$ ) to frequent extracellular stress over the course of 65 days. On average, parasites were passaged every 2.3 days, leaving parasites extracellular for ~32 hours in the presence or absence of continuous chloramphenicol selection. We also simultaneously passaged the original DiCre line (Andenmatten et al., 2013) under standard, non-stressing, culturing conditions. The new DiCre\_T2A line excision efficiency varied between 98 and 99% for replicates on day 1 and was maintained throughout the experiment with a maximal loss of 3% of excision efficiency, irrespective of the presence or absence of chloramphenicol selection, by day 65 (Fig. 2C). In contrast, the original DiCre line, cultured under standard non-stress conditions, lost 42% of excision capacity by day 65 (Supplementary Fig. 2), although this was only done as a single replicate. This shows that the second generation DiCre line, RH DiCre\_T2A  $\Delta ku80\Delta hxcgprt$ , retains high excision capacity over long periods of time, even when exposed to extracellular stress.

# **TgCAP is important but not essential for *in vitro* growth and deletion can be largely restored by the short cytoplasmic isoform, but only partially by the membrane bound isoform.**

To investigate CAP function, we generated a conditional knock out (cKO) of *CAP* using the DiCre strategy. Here, *CAP* with a C-terminal HA tag is flanked by two loxP sites, that recombine upon dimerisation of two split-Cre subunits, a process mediated by the small molecule rapamycin (RAP) (Andenmatten et al., 2013). To create the *CAP* conditional knockout line, we integrated a floxed, recodonised and HA-tagged *CAP* cDNA sequence into the endogenous locus of the RH DiCre $\Delta ku80\Delta hxcgprt$  line (Fig. 3A). Correct integration into the locus was confirmed by PCR (Fig. 3B). However, due to the DiCre issues detailed above, we were not able to successfully induce DiCre-mediated excision of the *CAP* gene. As the DiCre\_T2A strategy demonstrated consistently high excision rates over time, during our testing with a reporter construct, we integrated the DiCre\_T2A construct into the *KU80* locus of the non-excising floxed *CAP* parasite strain. This generated the parasite line RH DiCre\_T2A DiCre $\Delta ku80\Delta hxcgprt$  *LoxPCAP-HA*, called LoxPCAP hereafter. As expected, LoxPCAP displayed dual localisation by IFA (Fig. 3C). RAP treatment resulted in a complete loss of CAP ( $\Delta$ CAP), as shown by IFA (Fig. 3C) and Western blot (Fig. 3D).

To assess the requirements of CAP and its isoforms for various *Toxoplasma* functions, we complemented LoxPCAP parasites with either wildtype, the short or the long CAP isoform by integration of HA-tagged variants into the *UPRT* locus to generate merodiploid lines (named LoxPCAP<sup>CAP</sup>, LoxPCAP<sup>shortCAP</sup> and LoxPCAP<sup>longCAP</sup>, respectively). We then excised the endogenous *CAP* copy by RAP treatment. Clones were subsequently obtained by limiting dilution and excision verified by PCR (Supplementary Fig. 3).

This resulted in parasite strains that express only the WT complemented form ( $\Delta$ CAP<sup>CAP</sup>), the short complemented form ( $\Delta$ CAP<sup>shortCAP</sup>) or the long complemented form ( $\Delta$ CAP<sup>longCAP</sup>). We confirmed the differential localisation and translation of these isoforms by IFA (Fig. 3E) and Western blot (Fig. 3F). No differences in the protein levels of the two CAP isoforms could be

observed in the CAP complemented strain ( $\Delta\text{CAP}^{\text{CAP}}$ ) over the first 24 hours following host cell invasion, relative to the loading control (Supplementary Fig. 4).

To reliably quantify the contribution of CAP, and its two isoforms independently, to the lytic cycle, we performed a competition assay in which growth of  $\Delta\text{CAP}^{\text{CAP}}$  was compared to  $\Delta\text{CAP}$ ,  $\Delta\text{CAP}^{\text{shortCAP}}$  and  $\Delta\text{CAP}^{\text{longCAP}}$ . To do so, we integrated an mCherry expressing cassette into the  $\Delta ku80$  locus, replacing the DiCre\_T2A cassette in each of these lines. Note, the DiCre\_T2A cassette was no longer required because CAP had already been excised in these parasites. After 15 days in growth competition with  $\Delta\text{CAP}^{\text{CAP}}$ ,  $\Delta\text{CAP}$  parasites were largely depleted (>97.3%) from the population, while  $\Delta\text{CAP}^{\text{shortCAP}}$  showed a reduction of only 4%. In contrast,  $\Delta\text{CAP}^{\text{longCAP}}$  showed an intermediate level of depletion (33.3%). These phenotypes were exaggerated after 30 days in culture;  $\Delta\text{CAP}$  parasites were largely depleted (>99.9%),  $\Delta\text{CAP}^{\text{shortCAP}}$  showed a reduction of 12.4%, and  $\Delta\text{CAP}^{\text{longCAP}}$  growth was reduced by 43.1% relative to  $\Delta\text{CAP}^{\text{CAP}}$  (Fig. 4A). Collectively, these findings demonstrate that CAP plays an important but non-essential role in cell culture and that its function can be largely restored by the short CAP isoform but only partially by the long isoform.

### **TgCAP contributes to motility, invasion, egress and dense granule trafficking**

While the competition assays highlight the importance of CAP during the *in vitro* lytic cycle, they do not clarify which step of the cycle is affected. To test whether the growth differences between the lines were merely a result of differences in parasite replication rates, we counted the parasites per vacuole for each parasite line. No significant differences were observed (Supplementary Fig. 5). As CAP is a predicted actin regulator, we next focused our phenotypic analysis on *Toxoplasma* processes for which actin is known to be important, such as motility, egress, invasion and dense granule trafficking (Heaslip et al., 2016; Periz et al., 2017; Whitelaw et al., 2017).

In the absence of CAP ( $\Delta\text{CAP}$ ) significantly fewer parasites are able to initiate gliding motility in 3D motility assays (Leung et al., 2014) compared to the RH strain (Fig. 4B). In the motile population, trajectory displacement, trajectory length and maximum achieved speeds were all significantly reduced, although mean speed was not significantly different (Fig. 4B). To determine which isoform(s) contribute to parasite 3D motility, the motility parameters of  $\Delta\text{CAP}^{\text{CAP}}$ ,  $\Delta\text{CAP}^{\text{shortCAP}}$  and  $\Delta\text{CAP}^{\text{longCAP}}$  were compared. Both  $\Delta\text{CAP}^{\text{shortCAP}}$  and  $\Delta\text{CAP}^{\text{longCAP}}$  parasites showed similar levels of motility initiation, track displacement, track lengths and speed compared to  $\Delta\text{CAP}^{\text{CAP}}$  (Supplementary Fig. 6). These data indicate that CAP plays a role in initiation of motility and in controlling speed and track length once motile. Complementation with single isoforms shows that initiation of motility can be rescued by either CAP isoform and, once motile, either can maintain speed and track length.

As invasion and egress of host cells rely on active motility, we next compared invasion efficiency of  $\Delta\text{CAP}$  and the different complementation lines.  $\Delta\text{CAP}$  showed a significant reduction of invasion capacity (50.2% reduction compared to WT complemented lines), which was restored by both the short and long isoforms (Fig. 4C). We also performed egress assays in the presence of BIPPO, which results in a strong calcium response in *Toxoplasma* parasites causing synchronised and rapid egress from host cells (Howard et al., 2015).  $\Delta\text{CAP}$  parasites showed a substantial delay in egress from host cells at 30 s after induction (73.1% less egress in  $\Delta\text{CAP}$  compared to  $\Delta\text{CAP}^{\text{CAP}}$ ), while at 2 minutes the majority of parasites have egressed (10.6% less egress in  $\Delta\text{CAP}$  compared to  $\Delta\text{CAP}^{\text{CAP}}$ ) (Fig. 4D). This defect was fully restored in  $\Delta\text{CAP}^{\text{shortCAP}}$  parasites, while  $\Delta\text{CAP}^{\text{longCAP}}$  showed slightly lower levels of egress after 30 s of treatment but by 60 s were indistinguishable from WT or short CAP complemented lines. We also observed live egress events in which  $\Delta\text{CAP}$ , following host cell egress, showed decreased movement away from the host cell when compared to  $\Delta\text{CAP}^{\text{CAP}}$ ,  $\Delta\text{CAP}^{\text{shortCAP}}$  and  $\Delta\text{CAP}^{\text{longCAP}}$  (Videos 1-4).

A recent study revealed that directed dense granule transport is dependent on filamentous actin (Heaslip et al., 2016). Therefore, dense granule trafficking was assessed in  $\Delta$ CAP and the three complemented lines. We measured the run frequency (# of directed runs/parasite/minute), run length and velocity of directed motions. (Fig. 4E). Both the mean run length and the mean velocity were significantly increased in  $\Delta$ CAP (34.8% and 52.9%, respectively), but not in either of the complements. However, the frequency of directed runs was reduced in  $\Delta$ CAP (14.8%), but did not reach significance. These results indicate that both CAP isoforms play a supporting role in dense granule trafficking and that, upon CAP deletion, dense granules are trafficked further distances at higher speed. Collectively these data show that CAP plays a role in the actin-dependent processes described above and that either isoform is able to fulfil these CAP functions.

### **$\Delta$ CAP parasites display a defect in efficient cell-cell communication**

Actin, formin 3 and myosin I and J have been shown to be important for both parasite rosette organisation and cell-cell communication, as assessed by measuring the rapid transfer of reporter proteins between individual parasites in a vacuole (Frénal, Jacot, et al., 2017; Periz et al., 2017; Tosetti et al., 2019). Upon CAP deletion, we observed a complete loss of the characteristic rosette formation normally seen in *Toxoplasma*. This aberrant phenotype was fully rescued upon complementation with either WT CAP or the short CAP isoform (Fig. 5A).  $\Delta$ CAP<sup>longCAP</sup> displayed partial restoration with 44.9% of parasites forming phenotypically normal rosettes while the remainder were disorganised within the vacuole. This was also shown by scanning electron images of infected human fibroblasts in which the host cell and the vacuole membrane was removed (“unroofed”) as previously described (Magno et al., 2005) (Supplementary Fig. 7).

It was previously shown that mutant parasite lines which lost rosetting capacity also lost the rapid transfer of reporter proteins (called RTORP hereafter) between them. This has been established by photobleaching of individual parasites in a vacuole, which express a fluorescent reporter protein. Under normal conditions, all parasites in a vacuole contribute to the fluorescence recovery of the photobleached parasite (Frénal, Jacot, et al., 2017; Periz et al., 2017; Foe et al., 2018; Tosetti et al., 2019). Such transfer of reporter proteins has previously been used as a readout for cell-cell communication and, by extension, parasite connectivity (Frénal, Jacot, et al., 2017; Periz et al., 2017). To examine whether loss of cell-cell communication also accompanied the disrupted rosetting observed in  $\Delta$ CAP parasites, we performed fluorescence recovery after photobleaching (FRAP) experiments on  $\Delta$ CAP and its complementation lines. We chose vacuoles that contained 8 parasites/ vacuole as at this stage parasites organise in rosettes and individual cells can be easily monitored. We bleached one parasite in the vacuole and recorded both the recovery of fluorescence in the bleached parasite and the fluorescence levels of all other parasites in the vacuole. As expected, the WT-complemented  $\Delta$ CAP<sup>CAP</sup> photobleached parasites display rapid recovery of fluorescence to which, in most cases, all parasites in the vacuole appear to contribute (Fig. 5Bi, 5C and Video 5). Conversely,  $\Delta$ CAP photobleached parasites were supported in their rapid fluorescence recovery predominantly by just one other parasite, usually the parasite closest to the bleached cell, resulting in slow recovery (Fig. 5Bii, 5C and Video 6). In some cases, no recovery was observed in  $\Delta$ CAP parasites.

Loss of rapid protein transfer between parasites could be explained by a structural disruption of inter-parasite connections provided by the residual body. However, in addition to the residual body, an intravacuolar network (IVN) of tubule-like structures is present in the parasitophorous vacuole. Because of its tubular structure, it could also be involved in cell-cell communication. To determine whether the observed defect in the RTORP was dependent on the presence of the IVN, we performed a FRAP assay in RH  $\Delta$ ku80 $\Delta$ gra2 parasites (Rommereim et al., 2016) where the IVN fails to form but parasites still organise in rosettes. The results show that RTORP between parasites was not negatively affected (Fig. 5Biii and Video 7). The IVN, therefore, is unlikely involved in cell-cell communication.

To test if CAP deletion leads to a defect in cell-cell communication directly, or whether this is a direct consequence of the inability to form rosettes, we tested whether the RTORP varied between rosetting (r) and non-rosetting parasites (nr) of the  $\Delta\text{CAP}^{\text{longCAP}}$  line. These experiments revealed that if  $\Delta\text{CAP}^{\text{longCAP}}$  parasites rosette, they show normal RTORP between all cells in the vacuole, while non-rosetting parasites display the same defect as the  $\Delta\text{CAP}$  line, with fluorescence recovery from only one other parasite in the vacuole (Fig. 5C). Interestingly,  $\Delta\text{gra2}$  vacuoles showed a slight increase in the frequency of photobleach recovery from multiple parasites, but we have not further investigated this phenomenon here. The connectivity of parasites was also assessed based on the percentage of recovery after photobleaching. As expected,  $\Delta\text{CAP}$  and non-rosetting  $\Delta\text{CAP}^{\text{longCAP}}$  photobleached parasites recovered significantly less fluorescence than their rosetting counterparts (Fig. 5D).

Next, we sequentially photobleached individual  $\Delta\text{CAP}$  parasites in a vacuole and identified which parasites appear to be physically connected based on the transfer of mCherry (Fig. 5E). This revealed that only parasite pairs in close proximity are rapidly communicating. Collectively the results show that CAP deletion leads to a loss of both rosetting and the rapid transfer of reporter proteins between more than two parasites. Furthermore, RTORP appears to be dependent on parasite rosette organisation, but not on presence of the IVN.

#### **$\Delta\text{CAP}$ parasites have a defect in daughter cell orientation but not in synchronised division or apicoplast inheritance**

Previously, cell-cell communication has been hypothesised to control synchronous division between parasites within the same vacuole (Frénal, Jacot, et al., 2017). To determine whether  $\Delta\text{CAP}$  parasites display phenotypes previously observed for mutants with defective cell-cell communication, we used IMC3 antibodies to visualise synchronicity of forming daughter cells (Fig. 6A). Surprisingly,  $\Delta\text{CAP}$  vacuoles exhibited synchronous division with no significant difference to the WT complemented line (Fig. 6B). IMC3 staining was also used to assess daughter cell orientation. While in WT CAP complemented parasites 94.6% of daughter cells grew in the same orientation, a significant defect was observed in  $\Delta\text{CAP}$  and  $\Delta\text{CAP}^{\text{longCAP}}$  strains; only 42.9% ( $\Delta\text{CAP}$ ) and 67.7% ( $\Delta\text{CAP}^{\text{longCAP}}$ ) of daughter cells orientated in the same direction.  $\Delta\text{CAP}^{\text{shortCAP}}$  parasites were able to largely overcome this defect, with 89.5% of daughter cells growing in the same orientation (Fig. 6C). Such improper orientation of daughter cells following budding raises the possibility of improper organelle segregation too. To test this, we looked at apicoplast segregation, another actin-dependent process (Andenmatten et al., 2013; Jacot et al., 2013). Using streptavidin as a marker for the apicoplast, we identified no significant differences in apicoplast inheritance rates between  $\Delta\text{CAP}^{\text{CAP}}$  and  $\Delta\text{CAP}$  strains (Supplementary Fig. 8). These data show that despite a loss of rosette organisation and RTORP between parasites in a  $\Delta\text{CAP}$  vacuole, as well as disordered daughter cell orientation, parasite division remains synchronous. Furthermore, while CAP is supporting many actin-dependent processes in *Toxoplasma*, it appears dispensable for apicoplast division.

#### **CAP deletion leads to the formation of a decentralised residual body in which all parasites remain connected, despite loss of RTORP**

The observed synchronicity of division in the  $\Delta\text{CAP}$  strain, despite loss of RTORP, was unexpected. It suggested that synchronicity is either independent of the residual body, or that  $\Delta\text{CAP}$  parasites actually maintain connections that allow flow of proteins or metabolites to synchronise divisions. To investigate this, we established a connectivity map of parasites in a vacuole using correlative light and electron microscopy (CLEM). This allowed us to first analyse connectivity of parasites based on FRAP analysis, and then reconstruct a 3D electron microscopy image of the parasites and their connections by focused ion beam scanning electron microscopy (FIB SEM).

In the  $\Delta\text{CAP}^{\text{CAP}}$  strain, as expected for a WT complemented line, all parasites in the vacuole contribute to recovery of a photobleached parasite (Fig. 7A) and a normal residual body is



formed, connecting all parasites in the vacuole (Fig. 7B and Video 8), with one tubular extension extending away from the residual body with no apparent connections at the distal end. In contrast, for the  $\Delta$ CAP strain, fluorescence recovery of the photobleached parasite was predominantly observed from those cells in close proximity (Fig. 7C). To investigate how these parasites are connected, we analysed FIB SEM images obtained from the photobleached vacuole in Fig. 7C. This revealed membrane bound tubular connections of approximately 300 nm thickness between parasites, despite the aberrant transfer of mCherry and loss of rosetting (Fig. 7Di and ii). Following the lumen of the connections across 3 dimensions demonstrates that all parasites in the vacuole are connected by these tubular connections, likely representing a decentralised residual body that forms as a result of an inability to keep the posterior ends of the parasites in close proximity (Fig. 7D.iii, Supplementary Fig. 9 and Video 9). Correlation of the FRAP data with the FIB SEM images showed that rapid transfer of mCherry was always between parasites in close proximity at their basal ends.

While  $\Delta$ CAP parasites appear to be connected via a decentralised residual body, it could be that transfer of material through these connections is limited by physical barriers, such as the mitochondria which have previously been observed in the residual body (Frénal, Jacot, et al., 2017). Close examination of the residual body connections showed only one such connection contained two mitochondria and a constriction of the decentralised residual body lumen to ~50 nm, while all other connections appeared free of large physical barriers, indicating that this is unlikely an explanation for the lack of RTORP between parasites. However, we observed a complex network of tubules and sheet-like structures, likely representing the endoplasmic reticulum, in the connections (Fig. 7E) (Puhka et al., 2012; Schroeder et al., 2019; Tomavo et al., 2013; West et al., 2011). One of these tubular structures, tracked in three dimensions, was shown to enter multiple parasites via the basal pole, suggesting a possible continuum between them, which was also observed in then WT CAP complemented parasites. This has not been further examined here but could contribute to exchange of material between parasites.

Collectively, while CAP is important for rosette organisation of parasites, it is not essential for forming and sustaining a residual body with connectivity to all parasites in the vacuole. Furthermore, it shows that the RTORP is not an indicator of parasite connectivity.

### **Deletion of CAP results in completely avirulent type II parasites, but not in the type I RH strain.**

The short CAP isoform complements most phenotypes in cell culture while the long CAP isoform, in most cases, only shows a partial rescue. This raises the question about the evolutionary roles of the two different isoforms. To better discriminate the functions of the short and longCAP isoforms, we wanted to examine their respective roles in natural infections, where parasites encounter a number of additional stresses, including shear stress and the immune system. Accordingly, we addressed the essentiality of CAP and its isoforms in mouse infections. We hypothesised that if both isoforms are essential for parasite survival in a natural host, loss of either of the two isoforms would manifest in a fitness cost. First, we injected male C57BL/6 mice with ~25  $\Delta$ CAP or  $\Delta$ CAP<sup>CAP</sup> tachyzoites of the virulent RH strain, and monitored them over the course of 10 days. In both instances mice began to succumb to infection after 9 days, indicating that, despite the motility and rosetting phenotypes, CAP depletion in a type I RH background still results in high virulence in mice (Fig. 8A). As RH parasites have frequently been associated with hypervirulence and do not form cysts *in vivo*, we next generated  $\Delta$ CAP parasites and complemented versions in the type II Pru strain. In stark contrast to the RH line, upon injection of ~50,000 tachyzoites, Pru  $\Delta$ CAP parasites showed no virulence in mice while the Pru  $\Delta$ CAP<sup>CAP</sup>, Pru  $\Delta$ CAP<sup>shortCAP</sup>, and Pru  $\Delta$ CAP<sup>longCAP</sup> complemented parasites led to a lethal infection, with most mice succumbing to the parasites 8-10 days post-infection (Fig. 8B). These data show that expression of either individual isoform is sufficient to cause a lethal infection. Next, to look at formation of tissue cysts, which leads to a chronic infection, we injected a lower dose of ~5,000 tachyzoites of the Pru lines into mice. The majority of mice survived until day 32 post-infection, although 2  $\Delta$ CAP<sup>CAP</sup>-infected mice and 1  $\Delta$ CAP<sup>shortCAP</sup>-infected mouse died

before reaching this end-point. At day 32, the mice were sacrificed, brain samples were collected and serum tested for anti-*Toxoplasma* antibodies, confirming that all mice were successfully infected with *Toxoplasma* (Fig. 8C). Both the Pru  $\Delta$ CAP and Pru  $\Delta$ CAP<sup>longCAP</sup> infections demonstrated significantly lower cyst loads compared to Pru  $\Delta$ CAP<sup>CAP</sup> and Pru  $\Delta$ CAP<sup>shortCAP</sup> infected mice (Fig. 8D). These results show that CAP plays an essential role in the virulence of the type II Pru parasite strain, but not the type I RH strain. Moreover, while the short CAP isoform is able to fulfil all functions of TgCAP in cell culture and in the mouse model, the long isoform, despite its ability to complement most phenotypes to at least ~50% of WT complement levels, has a significant defect in establishing a chronic infection at the infectious dose used here.

## Discussion

*Toxoplasma* actin is important for a range of cellular processes, from organelle segregation and cell-cell communication, to gliding motility: a crucial factor in parasite dissemination (Andenmatten et al., 2013; Egarter et al., 2014; Periz et al., 2017). Despite the key role of actin in parasite biology, our understanding of actin dynamics and its regulation remains incomplete. CAP is a ubiquitous protein with a conserved role in regulating actin dynamics. In this study, we established that *Toxoplasma* CAP is expressed by an alternative translation initiation site, giving rise to two independent isoforms: shortCAP and longCAP. Through sequence alignment we identified that the alternate translation initiation site is conserved only within *Toxoplasma*, *Neospora* and *Hammondia*. These are all members of the Toxoplasmatinae, a subfamily of the Apicomplexa phylum, suggesting that while CAP is present in all apicomplexa, the long isoform is specific to *Toxoplasma* and its closest relatives. Here we investigated the role of both CAP isoforms in the *Toxoplasma* lytic cycle. Through *in vitro* competition assays, we show that complementation with shortCAP is enough to overcome the majority (87.6%), but not all, of the growth defect associated with CAP depletion. This suggests that longCAP is performing a specific function important for parasite fitness, which shortCAP is unable to compensate for. Furthermore, longCAP complementation restored 56.9% of the growth defect, arguing for a degree of functional overlap between the two isoforms. Our experiments have not uncovered a phenotype that only longCAP can rescue, which would have revealed a unique function. Its apical localisation, however, makes it tempting to speculate a function in actin regulation during invasion, which is a phenotype it can fully rescue. It could be that higher actin turnover is required at the apex and the concentration of longCAP here is fulfilling this need by influencing G-actin levels. Indeed, it has previously been hypothesised in other organisms that increased local concentration of CAP results in the sequestration of actin monomers (Ono, 2013). However, providing evidence for this hypothesis is limited by the fact that the shortCAP isoform can fully rescue all phenotypes in cell culture under the conditions tested. Given that cell culture assays do not fully represent the environment *Toxoplasma* normally encounters, we aimed to tease apart the functions of the two isoforms in mice. Surprisingly, even here the short isoform appears able to compensate for the lack of longCAP. This suggests that even under conditions encountered in the natural host, the longCAP isoform plays only a minor role, although dosage effects or routes of infection may well be confounding factors when assessing virulence of the different strains. Competition experiments between the mutants *in vivo* may help to tease apart the independent importance of the isoforms in the future. However, from the *in vitro* competition assays it can be predicted that parasites expressing two isoforms fare better than those expressing just one isoform. We cannot rule out that the differences in proteins levels of longCAP and shortCAP in the single isoform producing lines are affecting the phenotypic observations. However, both isoforms are able to rescue most phenotypes indicating that the protein levels do not appear to substantially affect CAP function.

Despite being dispensable for type I RH parasite virulence, CAP is essential for type II Pru parasite virulence in mice, and complementation with either shortCAP or longCAP restored lethality. At lower, non-lethal doses, longCAP complementation led to markedly reduced cyst formation in the brain. The underlying basis for this has not been explored here and it could be that it is the reduced fitness of the strain, rather than stage conversion phenotype, that causes

a reduction of parasites reaching the brain. Therefore, the observed virulence of the longCAP complemented strain is possibly due to the high dosage used, allowing the parasite to proliferate at high enough rates to overwhelm the immune system. Nevertheless, the basis for reduced fitness of  $\Delta$ CAP and  $\Delta$ CAP<sup>longCAP</sup> parasites in the murine infection model is likely multifactorial and we hypothesise that other actin-dependent processes that we have not assayed here could also contribute to the reduced virulence in mice.

The most pronounced phenotype of CAP deletion is loss of rosetting: the highly symmetrical physical distribution of parasites within the vacuole. Previous studies on actin, myosin I, myosin J, ADF and formin 3 have suggested that the actomyosin motor is important for rosetting (Frénal, Dubremetz, et al., 2017; Haase et al., 2015; Periz et al., 2017; Tosetti et al., 2019). Our  $\Delta$ CAP data further supports this hypothesis. Interestingly, complementing  $\Delta$ CAP parasites with longCAP restored rosetting in just under half of all vacuoles, with the remainder appearing as equally disordered as the  $\Delta$ CAP vacuoles. Despite this mixed population, we did not observe vacuoles with a combination of organised and disorganised parasites, suggesting rosetting is a binary outcome; either all parasites in a vacuole are connected by a central residual body, or not. This may suggest that the ability to produce highly organised rosettes is established during the first round of cell division when the residual body forms. This mixed population of rosetting and non-rosetting parasites, in an isogenic strain, gave us a unique opportunity to determine whether rosetting is important for efficient intravacuolar cell-cell communication. Using longCAP complemented parasites, we show that in rosetting vacuoles there is efficient RTORP with all parasites able to transfer material to the bleached parasite. Within the same population, non-rosetting vacuoles displayed severe defects in the RTORP with parasites seemingly only communicating in pairs. However, despite apparently only communicating in pairs, all parasites in the vacuole remained synchronised in their stage of replication. This is different to other studies which suggested that defects in RTORP between parasites leads to asynchrony in division (Frénal, Jacot, et al., 2017; Periz et al., 2017). Our results show that neither RTORP between daughter cells nor the formation of a rosette are predictors for synchronicity of division.

The synchronous division in  $\Delta$ CAP parasites could be explained by our FIB SEM results. Despite their disorganised appearance and loss of rapid cell-cell communication,  $\Delta$ CAP parasites are still connected by a decentralised residual body. This connection, although not facilitating rapid transfer of proteins between parasites that are further apart, could allow for slow or minimal transfer of proteins which is sufficient to synchronise divisions. An alternative hypothesis could be that metabolites, not proteins, are required to synchronise divisions, and their diffusion through the decentralised residual body is quicker. It is also a possibility that the seemingly continuous ER in the residual body, observed here connecting most if not all parasites, could contribute to synchronicity of division. Whatever the basis for synchronicity is, rosetting and rapid cell-cell communication are not essential and their analysis cannot be reliably used to predict whether connections between parasites exist. Recently, Foe *et al* reported that upon deletion of *ASH4*, a serine hydrolase, parasites were only connected in pairs but retained synchronicity of division (Foe et al., 2018), similar to our results. An explanation could be that *ASH4* mutants display a phenotype similar to the CAP phenotype described here, where, despite the loss of RTORP, parasites remain connected by a decentralised residual body, allowing synchronicity of division.

In summary, our results strongly support an actin regulatory role for CAP in *Toxoplasma*. Interestingly, actin dependent processes were affected to differing extents in  $\Delta$ CAP parasites, such as rosetting being completely lost while apicoplast inheritance was unaffected. This surely reflects the different spatial requirements for actin turnover within a cell. It is likely that the local concentration of actin, actin binding proteins such as the formins and the different myosins facilitate this. The results obtained here also leave open a few questions that are interesting to study in the future. How does actin help to initiate and maintain the centralised residual body? How are ER connections between parasites in a decentralised residual body

maintained and what is the function of this connection? What is the functional role of longCAP with its high concentration at the apex of the parasite? Why are some actin dependent processes completely reliant on CAP while others are not? Each of these questions will require careful analysis and the cell lines described here will likely provide useful tools to investigate these in the future.

## Materials and methods

### **Plasmid construction**

All primers used in this study are listed in Supplementary File 1. All synthetic DNA used in this study is listed in Supplementary File 2.

To generate the CAP-GFP fusion plasmid, pUPRT\_CAP\_GFP, the *Toxoplasma* CAP gene (TGME49\_310030) 5'UTR was amplified from genomic DNA using primer pair P1/P2 and Gibson assembled (Gibson et al., 2010) with a synthetic CAP cDNA-XmaI-eGFP sequence (GeneArt strings, Life Technologies, Massachusetts, United States) into *Bam*HI and *Pac*I digested UPRT targeting vector pUPRT-HA (Reese et al., 2011).

To generate the CAP cKO plasmid, pG140\_CAP\_cKO\_LoxP111, the CAP 5'UTR with a LoxP site inserted 111 bp upstream of the CAP start codon, and a recodonised CAP cDNA-HA sequence, were synthesised (GeneArt strings, Life Technologies). These DNA fragments were Gibson cloned (Gibson et al., 2010) into the parental vector p5RT70loxPKillerRedloxPYFP-HX (Andenmatten et al., 2013) which had been digested using *Ap*al and *Pac*I, creating an intermediate plasmid. Next, the CAP 3'UTR was amplified from genomic DNA using primer pair P3/P4 while mCherry flanked by *GRA* gene UTRs was amplified from pTKO2c (Caffaro et al., 2013) using primers P5/P6. These PCR products were Gibson cloned (Gibson et al., 2010) into the *Sac*I digested intermediate plasmid to create pG140\_CAP\_cKO\_LoxP111.

To generate pUPRT\_CAP, the CAP 5'UTR was amplified from genomic DNA using primer pair P1/P2. This DNA fragment and a synthetic CAP cDNA-*Bam*HI-HA sequence (GeneArt strings, Life Technologies), were Gibson cloned (Gibson et al., 2010) into *Bam*HI and *Pac*I digested UPRT targeting vector pUPRT-HA (Reese et al., 2011).

To generate pUPRT\_CAP\_C6,8A, the CAP 5'UTR was amplified from genomic DNA using primer pair P1/P2 and, alongside a synthetic CAP cDNA-HA sequence with C6,8A mutations (GeneArt strings, Life Technologies), was Gibson cloned (Gibson et al., 2010) into *Bam*HI and *Pac*I digested UPRT targeting vector pUPRT-HA (Reese et al., 2011).

To generate pUPRT\_CAP\_M1L, pUPRT\_CAP was amplified with primer pair P7/P8 to introduce the M1L point mutation.

To generate pUPRT\_CAP\_M37L, pUPRT\_CAP was amplified with primer pair P9/P10 to introduce the M37L point mutation.

To generate pG140\_DiCre, the plasmid containing DiCre\_T2A, two synthetic DNA fragments were produced containing *Ku80* homology region-alpha-tubulin promoter-FRB-Cre60-T2A-chloramphenicol resistance cassette-T2A-FKBP-Cre59-SAG1 3'UTR-*Ku80* homology region (gBlock gene fragments, Integrated DNA Technologies, Iowa, United States). These DNA fragments were Gibson cloned (Gibson et al., 2010) (into *Ap*al and *Sac*I digested parental vector, p5RT70loxPKillerRedloxPYFP-HX (Andenmatten et al., 2013)

To generate plasmids expressing CAS9 and a single guide RNA (sgRNA), we used plasmid pSAG1::CAS9-U6::sgUPRT as a backbone (Addgene plasmid #54467) (Shen et al., 2014). The plasmid was amplified with primer P11 and another containing a sgRNA to replace the UPRT-targeting sgRNA. Guide RNA sequences were selected using the Eukaryotic Pathogen CRISPR gRNA Design Tool (Peng & Tarleton, 2015). All sgRNA-expressing plasmids used in



this study were generated by this strategy. The sgRNA-containing primers are listed in Supplementary File 1.

For creation of plasmids with multiple sgRNAs, first, two separate vectors, each with a sgRNA, were generated as described above using the parental vector pSAG1::CAS9-U6::sgUPRT. Then, primers P12/P13 were used to amplify one of the sgRNA regions which was Gibson cloned (Gibson et al., 2010) into the other *KpnI* and *XhoI* digested plasmid, creating a multiple sgRNA plasmid.

# **Culturing of parasites and host cells**

*T. gondii* tachyzoites were cultured in human foreskin fibroblasts (HFF) and in Dulbecco's modified Eagle's medium (DMEM) with GlutaMAX (Invitrogen, California, United States) supplemented with 10% fetal bovine serum and maintained at 37°C with 5% CO<sub>2</sub>.

# **Generation of parasite lines**

To generate the conditional *CAP* knockout strain (RH DiCre $\Delta ku80\Delta hxgp\text{rt}$ \_LoxCAP-HA, referred to here as LoxPCAP), first, the linearised plasmid pG140\_CAP\_cKO\_LoxP111, carrying the *HXGPRT* cassette, was transfected into the RH DiCre $\Delta ku80\Delta hxgp\text{rt}$  strain (Andenmatten et al., 2013). Resistant parasites were cloned. Next, the DiCre conditional knockout function of the strain was restored. The linearised pG140\_DiCre plasmid, carrying the chloramphenicol resistance cassette and homology with the *Ku80* UTRs, was transfected into the strain. To increase *Ku80*-specific insertion efficiency, a plasmid with multiple *Ku80*-targeting sgRNAs was generated as described above using primer pairs P11/P14 and P11/P15. Resistant parasites were cloned. Integration into the *CAP* endogenous locus was confirmed using primer pairs P16/P17 and P18/P19. Replacement of *CAP* gDNA was confirmed using primers P20/P21. Excision of the floxed *CAP* sequence was confirmed with primer pairs P16/P20.

To complement the LoxPCAP strain with *CAP*-expressing constructs, the linearised plasmid pUPRT\_CAP, pUPRT\_CAP\_M1L or pUPRT\_CAP\_M37L was transfected alongside pSAG1::CAS9-U6::sgUPRT. 5-fluorodeoxyuridine (FUDR) resistant parasites were cloned.

*CAP* was subsequently excised from the above strains by addition of 50 nM rapamycin in DMSO for 4 hr at 37°C with 5% CO<sub>2</sub>, before washout, and excised parasites were cloned. Next, to aid with experimentation, an mCherry fluorescent construct was integrated into the *Ku80* locus, replacing the present DiCre\_T2A construct. mCherry flanked by *GRA* UTRs was amplified from pG140\_CAP\_cKO\_LoxP111 using primer pair P22/P23 which also carries 30 bp homology with the *Ku80* locus. To increase *Ku80*-specific insertion efficiency, a plasmid with multiple *Ku80*-targeting sgRNAs was generated as described above using primer pairs P11/P24 and P11/P25 and co-transfected with the PCR product. A population of parasites expressing mCherry were sorted by flow cytometry using a BD Influx cell sorter (BD Biosciences). Parasites were subsequently cloned, generating the strains  $\Delta CAP$ ,  $\Delta CAP^{CAP}$ ,  $\Delta CAP^{shortCAP}$  and  $\Delta CAP^{longCAP}$ .

The Pru  $\Delta ku80\Delta cap$  strain was generated by amplifying the *HXGPRT* resistance cassette from the pG140\_CAP\_cKO\_LoxP111 plasmid using primer pair P26/P27. To direct insertion of the PCR product to the *CAP* locus, a plasmid with multiple *CAP*-targeting sgRNAs was generated as described above using primer pairs P11/P28 and P11/P29 and co-transfected with the PCR product. Resistant parasites were cloned. To complement the Pru  $\Delta ku80\Delta cap$  strain with *CAP*-expressing constructs, the linearised plasmid pUPRT\_CAP, pUPRT\_CAP\_M1L or pUPRT\_CAP\_M37L was transfected alongside pSAG1::CAS9-U6::sgUPRT. FUDR resistant parasites were cloned.

To generate fluorescent  $\Delta gra2$  parasites for FRAP experimentation, mCherry flanked by *GRA* UTRs was amplified from pG140\_CAP\_cKO\_LoxP111 using primer pair P30/P31 with *UPRT*

locus overhangs. This PCR product was co-transfected with pSAG1::CAS9-U6::sgUPRT into the RH  $\Delta ku80 \Delta gra2$  strain (Rommereim et al., 2016). An FUDR resistant population was obtained.

The RH DiCre\_T2A  $\Delta ku80 \Delta hxgprt$  line was generated by integrating the DiCre construct into the *Ku80* locus in RH  $\Delta ku80 \Delta hxgprt$  parasites (Huynh & Carruthers, 2009). The DiCre construct was amplified from pG140\_DiCre using primer pair P32/P33 which also carries 30 bp homology with the *Ku80* locus. To increase *Ku80*-specific insertion efficiency, a plasmid with a *Ku80*-targeting sgRNA was generated as described above using primer pairs P34/P11 and co-transfected with the PCR product. Resistant parasites were cloned.

To assess the efficiency of rapamycin-dependent excision of the DiCre strains, the Killer Red gene-swap construct was amplified from p5RT70loxPKillerRedloxPYFP-HX (Andenmatten et al., 2013) using primer pair P35/P36. This PCR product was co-transfected with pSAG1::CAS9-U6::sgUPRT for targeted insertion into the *UPRT* locus. FUDR resistant parasites were cloned.

To generate a CAP C-terminal endogenous HA-tagged line, a synthetic DNA repair template was produced containing CAP gDNA (a section of which is recodonised), a HA tag and the CAP 3'UTR (gBlock gene fragments, Integrated DNA Technologies). The DNA repair template was amplified using primer pair P37/P38. To direct insertion of the PCR product to the CAP locus, a plasmid with a single CAP-targeting sgRNA was generated as described above using the primer pairs P39/P11 and was co-transfected with the PCR product into RH  $\Delta ku80$  parasites. A population of parasites expressing the co-transfected Cas9-GFP-containing plasmid were sorted by flow cytometry using a BD Influx cell sorter (BD Biosciences). ~70% of these parasites expressed the HA peptide by IFA.

# **Parasite transfection and selection**

To generate stable transformants,  $0.5 - 1 \times 10^7$  freshly lysed parasites were transfected with either 25  $\mu$ g of linearised template DNA, 5  $\mu$ g of linearised template DNA and 20  $\mu$ g of a corresponding gRNA-specific CRISPR/CAS9 plasmid or template DNA produced from 1 ethanol precipitated PCR and 20  $\mu$ g of a corresponding gRNA-specific CRISPR/CAS9 plasmid. Selection on the basis of 5-fluorodeoxyuridine (20  $\mu$ M), mycophenolic acid (25  $\mu$ g ml<sup>-1</sup>), xanthine (50  $\mu$ g ml<sup>-1</sup>) or chloramphenicol (21  $\mu$ M) was performed according to the selection cassette used.

# **Preparation of parasite genomic DNA**

Genomic DNA was extracted from *T. gondii* tachyzoites to use as a PCR template by pelleting parasites and resuspending in PBS. DNA extraction was then performed using the Qiagen QIAamp DNA blood mini kit as per the manufacturer's protocol.

# **IFA**

Parasites were seeded onto HFFs grown on coverslips. 16 – 24 h after seeding, the coverslips were fixed in 3% formaldehyde for 15 min at room temperature then permeabilised in 0.2% Triton X-100/PBS for 3-10 min and blocked in 3% BSA/PBS for 1 h. Staining was performed using appropriate primary antibodies and goat Alexa Fluor 488-, Alexa Fluor 594- and Alexa Fluor 647-conjugated secondary antibodies (1:2000) alongside DAPI (5  $\mu$ g/ml). Coverslips were mounted on glass slides with SlowFade gold antifade mountant (Life Technologies). Antibody concentrations used were: rat anti-HA high affinity (Roche, Basel, Switzerland) (1:1000), rabbit anti-TgCAP (1:2000), mouse anti-GFP (Roche) (1:1000).

Widefield images were generated with a Ti-E Nikon microscope using a 63x or 100x objective (Tokyo, Japan). Images were processed with Nikon Elements software. Confocal images were taken using a Zeiss LSM-780 inverted confocal laser scanning microscope with a 63x objective. Images were processed with Zeiss Zen Black software (Oberkochen, Germany).

## Western blot

Western blot samples were obtained by scraping and lysing intracellular parasites in 200 µl 1x Laemmli buffer (2% SDS, 10% glycerol, 5% 2-mercaptoethanol, 0.002% bromophenol blue and 125 mM Tris HCl, pH 6.8). Samples were subjected to SDS-PAGE under reducing conditions before being transferred to a nitrocellulose membrane. Immunoblotting was performed with appropriate primary antibodies in 0.1% Tween 20, 3% skimmed milk/PBS. Bound secondary fluorochrome-conjugated antibodies were visualised using the Odyssey Infrared Imaging System (LI-COR Biosciences, Nebraska, United States).

Antibody concentrations used were: rat anti-HA high affinity (Roche) (1:1000), rabbit anti-TgCAP (1:2000), mouse anti-*Toxoplasma* [TP3] (Abcam, Cambridge, United Kingdom) (1:1000). Goat anti-mouse IRDye 800CW (LI-COR) (1:20000), Donkey anti-rabbit IRDye 680LT (LI-COR) (1:20000), Goat anti-rat IRDye 680LT (LI-COR) (1:20000).

## Generation of TgCAP antibody

To generate the shortCAP expression plasmid, pET-28\_CAP\_A38toC203, a *Toxoplasma* shortCAP (M37toC203) recodonised sequence was synthesised (gBlock gene fragments, Integrated DNA Technologies) and Gibson cloned (Gibson et al., 2010) into *Bam*HI and *Nde*I digested pET-28a(+) plasmid (Merck, Darmstadt, Germany). This allowed for expression of an N-terminal 6xHis tagged shortCAP recombinant protein in *Escherichia coli* BL21 cells under the control of T7 *lac* promoter. Short CAP was expressed and His tag purified using Ni-NTA affinity purification under native conditions using the standard manufacturer's protocol (Qiagen, Hilden, Germany). The shortCAP recombinant protein was used to immunize female New Zealand white rabbits (Covalab, Cambridge, United Kingdom) for generation of polyclonal antibodies.

## Flow cytometry analysis of DiCre excision

Parasites were added to a HFF monolayer and allowed to invade for 1 h. Then, cre recombinase-mediated recombination was induced by addition of 50 nM rapamycin in DMSO for 4 hr before washout. 22 h after infection, parasites were lysed, pelleted and washed twice in PBS. Parasites were resuspended in 0.5 ml 3% formaldehyde and fixed for 10 min. The suspension was centrifuged and the pellet washed in PBS before resuspension in PBS. To remove debris, samples were passed through a 30 µm pre-separation filter (Miltenyi Biotec, Bergisch Gladbach, Germany). 20,000 events were recorded using a BD LSR II flow cytometer (BD Biosciences California, United States). Killer Red was excited by the 561 nm laser and detected by a 600 long pass filter and either a 582/15, 610/20 or 620/40 band pass filter. YFP was excited by the 488 nm laser and detected a 505 long pass filter and either a 525/50 or 530/30 band pass filter. For quantification, and elimination of debris, total number of Killer Red+ parasites was considered 100%. This was performed at day 0, 35 and 65 of the experiment. For each condition, three biological replicates were analysed. At least 10000 Killer Red+ events were counted for each individual time point.

## Phenotypic characterisations

### Competition Assay

mCherry-expressing  $\Delta$ CAP,  $\Delta$ CAP<sup>CAP</sup>,  $\Delta$ CAP<sup>shortCAP</sup> or  $\Delta$ CAP<sup>longCAP</sup> parasites were mixed with non-fluorescent  $\Delta$ CAP<sup>CAP</sup> parasites at an average ratio of 60/40. At day 0, 15 and 30 in culture, the ratio was determined by flow cytometry for two biological replicates. Parasites were lysed, pelleted and washed twice in PBS. Parasites were resuspended in 0.5 ml 3% formaldehyde and fixed for 5 min. The suspension was centrifuged and the pellet resuspended in 5 µg/ml DAPI/PBS for 10 min. The pellet was washed and resuspended in PBS. To remove debris, samples were passed through a 30 µm pre-separation filter (Miltenyi Biotec). Events were recorded using a BD LSR II flow cytometer (BD Biosciences). DAPI was excited by the 355 nm laser and detected by a 450/50 band pass filter. mCherry was excited by the 561 nm laser and detected by a 600 long pass filter and a 610/20 band pass filter. To eliminate debris from

the analysis, events were gated on DAPI fluorescence. The ratio of control parasites (DAPI+/mCherry-) to individual CAP complements (DAPI+/mCherry+) was calculated and normalised to the day 0 ratio. The data represent two (day 15) and three (day 30) independent experiments. At least 1500 DAPI+ events were obtained for each individual time point. The results were statistically tested with a two-way ANOVA test plus a multiple comparison Sidak's test individually comparing day 15 or day 30 means to their respective day 0 mean, in GraphPad Prism® 7. The data presented are as mean  $\pm$  s.d.

### **Intracellular growth and rosetting assay**

Parasites were harvested from a T-25 and added to a coverslip coated with a HFF monolayer. After 20 h the coverslips were fixed with 3% formaldehyde for 15 min at room temperature. Coverslips were mounted and mCherry expression used to identify parasites. For each replicate, 4 random fields were imaged with a 40x objective. Counts were performed in a blinded manner in duplicate for two independent experiments. The number of parasites per vacuole was determined by counting at least 265 vacuoles per strain. The number of vacuoles that rosette was determined by looking at 8-pac vacuoles, at least 90 vacuoles per strain were counted. The results were statistically tested with a one-way ANOVA test plus a multiple comparison Dunnett's test comparing all means to the  $\Delta$ CAP<sup>CAP</sup> mean in GraphPad Prism® 7. The data presented are as mean  $\pm$  s.d.

### **Invasion assay**

Red/green invasion assays were performed. mCherry-expressing parasites were lysed in an invasion non-permissive buffer, Endo buffer (44.7 mM K<sub>2</sub>SO<sub>4</sub>, 10 mM MgSO<sub>4</sub>, 106 mM sucrose, 5 mM glucose, 20 mM Tris-H<sub>2</sub>SO<sub>4</sub>, 3.5 mg/ml BSA, pH 8.2). 250  $\mu$ l of  $8 \times 10^5$  parasites/ml in Endo buffer were added to each well of a 24-well flat-bottom plate [Falcon], which contains a coverslip with a confluent HFF monolayer. The plates were spun at 129 x g for 1 min at 37°C to deposit parasites onto the monolayer. The Endo buffer was gently removed and replaced with invasion permissive medium (1% FBS/DMEM). These parasites were allowed to invade for 1 min at 37°C after which the monolayer was gently washed twice with PBS and fixed with 3% formaldehyde for 15 min at room temperature. Extracellular parasites were stained with mouse anti-*Toxoplasma* antigen B1247M (Abcam) 1:1000 and goat anti-mouse Alexa Fluor 488, following the IFA protocol. For each replicate, 3 random fields were imaged with a 40x objective. Three independent experiments were performed in duplicate. The number of intracellular (mCherry+/488-) and extracellular (mCherry+/488+) parasites was determined by counting, in a blinded fashion, at least 758 parasites per strain. The results were statistically tested with a one-way ANOVA test plus a multiple comparison Dunnett's test comparing all means to the  $\Delta$ CAP<sup>CAP</sup> mean in GraphPad Prism® 7. The data presented are as mean  $\pm$  s.d.

### **Egress assay**

Parasites were added to a HFF monolayer, in a ibidi  $\mu$ -plate 96 well, and grown for 30 h. The wells were washed twice with PBS and the media was exchanged for 80  $\mu$ l Ringers solution (155 mM NaCl, 3 mM KCl, 2 mM CaCl<sub>2</sub>, 1 mM MgCl<sub>2</sub>, 3 mM NaH<sub>2</sub>PO<sub>4</sub>, 10 mM HEPES, 10 mM glucose). To artificially induce egress, 40  $\mu$ l of Ringer's solution containing 150  $\mu$ M BIPPO (50  $\mu$ M final conc) was added to each well. At specified time points the cells were fixed by adding 26  $\mu$ l 16% formaldehyde (3% final conc) for 15 min. Cells were washed in PBS and stained with DAPI (5  $\mu$ g/ml). Automated image acquisition of 25 fields per well was performed on a Cellomics Array Scan VTI HCS reader (Thermo Scientific, Massachusetts, United States) using a 20 $\times$  objective. Image analysis was performed using the Compartmental Analysis BioApplication on HCS Studio (Thermo Scientific). Egress levels were determined in triplicate for three independent assays. At least 11987 vacuoles per strain were counted at t = 0 s. Subsequent time point vacuole counts were normalised to t=0 to determine how many vacuoles had egressed. The results were statistically tested with a two-way ANOVA test plus



a multiple comparison Dunnett's test comparing all means to the  $\Delta\text{CAP}^{\text{CAP}}$  mean, at each time point separately, in GraphPad Prism® 7. The data presented are as mean  $\pm$  s.d.

### **Live egress**

Parasites were added to a HFF monolayer, in a ibidi  $\mu$ -plate 96 well, and grown for 30 h. The wells were washed twice with PBS and the media was exchanged for 80  $\mu$ l Ringers solution (155 mM NaCl, 3 mM KCl, 2 mM  $\text{CaCl}_2$ , 1 mM  $\text{MgCl}_2$ , 3 mM  $\text{NaH}_2\text{PO}_4$ , 10 mM HEPES, 10 mM glucose). The plate was then transferred to a Ti-E Nikon microscope with a 37°C environmental chamber. To artificially induce egress, 40  $\mu$ l of Ringer's solution containing 150  $\mu$ M BIPPO (50  $\mu$ M final conc) was added to each well after imaging had commenced. Images were captured every 1.8 s.

### **Apicoplast segregation assay**

Parasites were added to a HFF monolayer and grown for 20 h before fixation with ice cold methanol for 2 min at room temperature. IFAs were performed using a streptavidin-Alexa Fluor 594 conjugate (Invitrogen) as a marker for the apicoplast. Correct apicoplast segregation was determined in duplicate for three independent assays. At least 228 vacuoles were counted per strain. Counts were performed in a blinded manner. The results were statistically tested with an unpaired t test in GraphPad Prism® 7. The data presented are as mean  $\pm$  s.d.

### **Synchronicity of division and daughter cell orientation assay**

Parasites were added to a HFF monolayer and grown for 20 h before fixation with 3% formaldehyde for 15 min at room temperature. IFAs were performed using rat anti-IMC3 antibodies. To determine the synchronicity of cell division within the vacuoles, anti-IMC3 staining was used to evaluate the stage of daughter cell development. Vacuoles were scored as synchronous if all daughter cells were at the same stage of development. Vacuoles were counted blind in triplicate for three independent experiments. At least 275 vacuoles were counted per strain. The results were statistically tested with an unpaired t test in GraphPad Prism® 7. The data presented are as mean  $\pm$  s.d. Daughter cell orientation was quantified in triplicate for three independent experiments. At least 312 mother cells were counted blind, per strain. The results were statistically tested with a one-way ANOVA test plus a multiple comparison Dunnett's test comparing all means to the  $\Delta\text{CAP}^{\text{CAP}}$  mean in GraphPad Prism® 7. The data presented are as mean  $\pm$  s.d.

### **3D motility assay**

Motility assays were performed as previously described (Leung et al., 2014), with minor modifications. Parasites were syringe-released from a HFF monolayer (one heavily infected T75 flask per strain) by passing through a 27 gauge needle and filtering through a 3  $\mu$ m Nuclepore filter. Parasites were then centrifuged (1,000 x g for 2 min) and resuspended in 40  $\mu$ l motility media supplemented with 0.3 mg/mL Hoescht 33342. Matrigel was thawed on ice to prevent polymerization and combined with parasites and motility media in a ratio of 3:1:3 respectively. Pitta chambers were perfused with 10  $\mu$ l of this suspension and incubated at 27°C for 7 minutes on a thermoplate. Chambers were incubated in the heated (35°C  $\pm$  1°C) microscope enclosure for 3 min prior to imaging. Parasite nuclei were imaged, using a 20x objective, capturing 61 – 63 stacks of 41 z-slices 1  $\mu$ m apart. To ensure conditions remained constant between parasite lines, samples used for capture were alternated. Datasets were exported to Imaris x64 v9.2.1. Using the ImarisTrack module parasites were tracked in a region of interest from which 1  $\mu$ m has been cropped from the x and y edges to eliminate edge artefacts. Parasites were identified, after background subtraction, using spot detection with estimated size of 4  $\mu$ m (xy) and 8  $\mu$ m (z). Spots were filtered to exclude all that had duration of less than 3 seconds to minimise tracking artifacts. An autoregressive motion tracking algorithm was applied with a maximum distance of 6  $\mu$ m and a maximum gap size of 3. Datasets were manually inspected to ensure appropriate tracking and to remove artifacts and trajectories tracked from multiple identified spots. Percent moving was calculated as the

number of trajectories (>2  $\mu\text{m}$  displacement) / number of objects in frame 3 (>3 s duration). Trajectory parameters were extracted directly from Imaris software. Data shown are derived from 4 independent biological replicates, each consisting of a minimum of two technical replicates. For all analysis, means and standard deviation were calculated for four independent biological replicates before statistical analysis using an unpaired t-test in GraphPad Prism®7. For the three strain experiment,  $\Delta\text{CAP}^{\text{shortCAP}}$  and  $\Delta\text{CAP}^{\text{longCAP}}$  were each compared to  $\Delta\text{CAP}^{\text{CAP}}$ . All technical replicates are presented in the figures, together with their mean  $\pm$  s.d.

### Dense granule trafficking assay

For each condition  $1 \times 10^7$  parasites were transiently transfected with 30  $\mu\text{g}$  of pTub SAG1 $\Delta$ GPI-mCherry plasmid (Heaslip et al., 2016) and immediately added to a confluent HFF monolayer in a Mattek® 35 mm dish, coverslip 1.5. 12-15 h after infection the monolayers were washed 3 times with pre-warmed Gibco® Fluorobrite™ DMEM supplemented with 4% Fetal Bovine Serum. The coverslips were immediately used for imaging. The acquisitions were made with an Olympus IX71 coupled to a DELTAVISION™ Elite imaging system in a 37°C environmental chamber. The acquisition for each condition were made sequentially from the washing step to the acquisition with a random order to avoid any artifactual data. The acquisition analysis was made with Fiji and the MTrackJ plugin. The data represent three independent experiments. At least 43 parasites and 273 direct runs were counted per strain. The results were statistically tested with a one-way ANOVA test plus a multiple comparison Dunnett's test comparing all means to the  $\Delta\text{CAP}^{\text{CAP}}$  mean in GraphPad Prism® 7. The data presented are as mean  $\pm$  s.d.

### FRAP

Parasites were inoculated on a confluent layer of HFFs 20 h before experiments were performed using a Zeiss LSM-780 inverted confocal laser scanning microscope at 37°C. Acquisition and processing were performed with the Zeiss Zen Black software. Images were taken for 2 min (one image per second). Three pre-bleach images were recorded before the region of interest was photobleached ten times with a 561 nm laser at 100% power. Fluorescence intensity is presented as a percentage relative to the same area pre-bleach. These normalised intensity values were also used for the calculations below. To calculate percentage of fluorescence recovery, the final reading (116 s post-bleach) was subtracted from the reading immediately post-bleach,  $t = 3$  s, to give percentage recovery after 116 s. To calculate percentage loss of fluorescence, the reading immediately post-bleach,  $t = 3$  s, was subtracted from the final reading (116 s post-bleach) to give percentage loss after 116 s. These percentages were used to generate the heat map. At least 11 vacuoles were counted per strain across at least two independent experiments. The results were statistically tested with a one-way ANOVA test plus a multiple comparison Dunnett's test comparing all means to the  $\Delta\text{CAP}^{\text{CAP}}$  mean in GraphPad Prism® 7. The data presented are as mean  $\pm$  s.d. To assess recovery type, at least 11 vacuoles were counted per strain across at least two independent experiments. The results were statistically tested with a Chi-square in GraphPad Prism® 7.

### Tape unroofing SEM

Parasites were inoculated on a confluent HFF monolayer 24 h before fixation in EM fixative (2.5% glutaraldehyde, 4% formaldehyde in 0.1 M phosphate buffer) for 30 min. Cells were washed in 0.1 M phosphate buffer (PB) and stored in 1% formaldehyde in PB at 4°C. Cells were then washed in PB at room temperature, then washed in ddH<sub>2</sub>O at RT. The cells were dehydrated stepwise from 70% to 100% ethanol before critical point drying from acetone in a CPD300 (Leica Microsystems, Vienna, Austria). After drying, the coverslips were mounted on stubs, and the HFF cells were unroofed by placing Scotch tape on the coverslips and gently peeling it off, exposing the host cytoplasm and the parasitophorous vacuoles. The cells were coated with 7 nm platinum in a Q150R Sputter Coater (Quorum Tech, East Sussex, UK) before viewing in a Phenom ProX SEM (Thermo Scientific) at 10 kV, 1024 x 1024 pixel frame, on 'high' quality.

## FIB SEM

Immediately following FRAP experimentation, as described above, parasites were fixed in 4% formaldehyde for 15 min at 37°C before washing in 0.1 M PB. Cells were then fixed in EM fixative (2.5% glutaraldehyde, 4% formaldehyde in 0.1 M PB) for 30 min at room temperature. Cells were washed in 0.1 M PB and stored in 1% formaldehyde in 0.1 M PB. After fixation, samples were transferred to a Pelco BioWave Pro+ microwave (Ted Pella) for processing using a protocol adapted from the NCMIR protocol (Deerinck et al., 2010). See Supplementary File 3 for full BioWave program details. The SteadyTemp plate was set to 21°C unless otherwise indicated. Each step was performed in the microwave, except for the buffer and ddH<sub>2</sub>O wash steps, which consisted of two washes on the bench and two washes in the microwave (250 W for 40 s). The cells were washed (as above) in 0.1 M PB, stained with 2% osmium tetroxide and 1.5% potassium ferricyanide (v/v) for 14 min under vacuum (with/without 100 W power at 2 min intervals), and then washed in ddH<sub>2</sub>O (as above). Next, the cells were incubated in 1% thiocarbonylhydrazide in ddH<sub>2</sub>O (w/v) for 14 min (vacuum, 100 W on/off at 2 min intervals) with SteadyTemp plate set to 40°C, followed by ddH<sub>2</sub>O washes (as above), and then a further stain with 2% osmium tetroxide in ddH<sub>2</sub>O (w/v) for 14 min (vacuum, 100 W on/off at 2 min intervals), followed by ddH<sub>2</sub>O washes (as above). The cells were then incubated in 1% aqueous uranyl acetate (vacuum, 100 W on/off at 2 min intervals, SteadyTemp 40°C), and then washed in ddH<sub>2</sub>O (as above, except with SteadyTemp at 40°C). Walton's lead aspartate was then applied (vacuum, 100 W on/off at 2 min intervals, SteadyTemp 50°C), and the cells were washed (as above) and dehydrated in a graded ethanol series (70%, 90%, and 100%, twice each), at 250 W for 40 s without vacuum. Exchange into Durcupan ACM® resin (Sigma-Aldrich, Missouri, United States) was performed in 50% resin in ethanol, at 250 W for 3 min, with vacuum cycling (on/off at 30 sec intervals), and then pure Durcupan was infiltrated in four microwave steps with the same settings, before embedding at 60°C for 48 h.

Focused ion beam scanning electron microscopy (FIB SEM) data was collected using a Crossbeam 540 FIB SEM with Atlas 5 for 3-dimensional tomography acquisition (Zeiss). Segments of the cell monolayer containing the cells of interest were trimmed, polished with a diamond knife (removing uneven resin at the base of the monolayer to provide a flat surface for tracking marks), mounted on a standard 12.7 mm SEM stub using conductive epoxy (ITW Chemtronics), and coated with a 5 nm layer of platinum.

The specific cells of interest were relocated by imaging through the platinum coating at an accelerating voltage of 20 kV and correlating to previously acquired fluorescence microscopy images. After preparation for milling and tracking, images were acquired at 5 nm isotropic resolution throughout each region of interest, using a 10 µs dwell time. During acquisition the SEM was operated at an accelerating voltage of 1.5 kV with 1 nA current. The EsB detector was used with a grid voltage of 1,200 V. Ion beam milling was performed at an accelerating voltage of 30 kV and current of 700 pA.

After cropping to the specific region of interest comprising the entire extent of the PV ( $\Delta\text{CAP}^{\text{CAP}}$ ; 3080 x 634 x 2509 pixels; 15.4 x 3.17 x 12.545 µm;  $\Delta\text{CAP}$ ; 4065 x 1136 x 4490 pixels; 20.325 x 5.68 x 22.45 µm) and aligning the dataset (gradient align; Atlas 5), the images were processed to suppress noise and slightly enhance sharpness (gaussian blur 0.75 radius, followed by unsharp mask radius 1, strength 0.6; Fiji) prior to reorienting and reslicing in the YZ plane (assigned as the XY plane for segmentation), and scaling to 10 nm isotropic resolution for segmentation and display.

Selected structures were segmented manually from the FIB SEM datasets and 3D reconstructions were made using the 3dmod program of IMOD (Kremer et al., 1996). The normal and decentralised residual body structures were manually skeletonised by tracing the approximate central axis of the structure from the posterior pore of each tachyzoite using open contours. Thus, the green skeleton follows the lumen of the connections between parasites.

The minimum number of points were placed that would still ensure the contour remained at the central axis of the volume. Where the structure branched, points linking contours from multiple extensions were placed at the approximate centre of the branch point volume. The contours were then rendered as a 50 or 100 nm tube to aid visualisation (tube diameter chosen depending on view). This model was then inspected in the X, Y, and Z-planes and corrections made to ensure the skeleton followed the approximate centre through the volume. Since not all RB-like structure extensions ended at the posterior pole of a tachyzoite, the posterior poles were highlighted by segmenting them with open contours with points at every 40 nm in Z, following the edge of the cytosol (the ribosome-containing electron lucent space where it meets the intermediate electron density surrounding the inner membrane complex), and meshing the contour as a 50 nm tube. A selected region of the putative ER lipid bilayer outer leaflet was segmented with closed contours drawn every 5-20 nm in Z (smaller Z intervals where needed to capture fenestrations/complexity); from an approximately square region around the inner face of two of the basal pores up to an arbitrary point along the decentralised residual body structure. Contour gaps were placed at the edge of this region. Two tachyzoites were also highlighted by partial coarse segmentation; closed contours drawn every 250 nm in Z through the main body of the cell (segmentation of the complex top and bottom of the tachyzoites was omitted for clarity).

## Animals

C57BL/6 (wild type) mice were bred and housed under pathogen-free conditions in the biological research facility at the Francis Crick Institute in accordance with the Home Office UK Animals (Scientific Procedures) Act 1986. All work was approved by the UK Home Office (project license PDE274B7D), the Francis Crick Institute Ethical Review Panel, and conforms to European Union directive 2010/63/EU. All mice used in this study were male and between 7- to 9-week old.

Mice were infected with *T. gondii* tachyzoites by intraperitoneal injection (i.p.) with either  $25 \times 10^3$  parasites (cyst formation) or  $5 \times 10^4$  parasites (survival) in 200  $\mu$ l medium on day 0. Mice were monitored and weighed regularly for the duration of the experiments.

For serum samples, mice were euthanized and blood collected into blood serum collection tubes (SAI, Infusion technologies) by puncturing the jugular vein. Blood was allowed to clot at room temperature for 30 min, before tubes were centrifuged at 1500 x g for 10 min. Serum was collected and stored at -20°C until analysis.

## *Toxoplasma* serum antibody ELISA

*Toxoplasma* soluble antigens were extracted as previously described (Silva et al., 2007). In short, parasites were syringe-lysed, washed once with PBS, and adjusted to  $1 \times 10^8$  tachyzoites/ml with PBS containing protease inhibitors (cOmplete mini, Roche). Parasites were lysed by five freeze-thaw cycles (liquid nitrogen/37°C), followed by ultrasound sonication on ice (five 60 Hz cycle for 1 min each). Samples were centrifuged at 10,000 x g for 30 min at 4 °C before supernatants were collected and protein content was determined using the BCA Protein Assay Kit (Pierce, Thermo Fisher Scientific) following the manufacturer's instructions.

To detect *Toxoplasma* antibodies in murine serum samples, 96-well plates (flat bottom, high-binding) were coated overnight with 2  $\mu$ g/ml *Toxoplasma* soluble antigens at 4°C. Plates were washed with PBS/0.05% Tween-20 (v/v) (PBS-T) before blocked with 1% BSA (w/v) in PBS for 2 h at room temperature. Bound antigens were incubated with murine sera diluted 1/10 in 1% BSA/PBS for 2 h at room temperature, washed three times with PBS-T and bound antibodies detected by incubation for 2 h at room temperature with anti-mouse Immunoglobulins (HRP conjugate, Darko) diluted 1/1000 in 1% BSA/PBS. Finally, plates were washed three times with PBS-T and developed by adding TMB substrate solution (Thermo Fisher Scientific). The TMB reaction was stopped by adding 2 N sulphuric acid and the absorbance measured (OD<sub>450</sub> minus OD<sub>540</sub> wave length correction) using the VersaMax™ Microplate Reader with SoftMax® Pro Software.



# Mouse brain collection and preparation for cyst counting

To determine the number of cysts in the brain of infected animals, mice were euthanized and the brain extracted from the skull. The brain was homogenised in 1 ml PBS and stained with Rhodamine-conjugated *Dolichos biflorus* agglutinin (1/1000; Vector Laboratories) for 1 h at room temperature. Fluorescently labelled cysts were counted using a Ti-E Nikon microscope.

## Statistical analysis

Statistical tests used are stated in individual sections above. *P*-values significance thresholds were set at: \*\*\*\* *P* < 0.0001, \*\*\* *P* < 0.001, \*\* *P* < 0.01 and \* *P* < 0.05. All significant results are labelled with a line and asterisk(s) in the graphs.

## Acknowledgements

We thank Marc-Jan Gubbels (Boston College) for gifting the IMC3 antibody, Markus Meissner (University of Glasgow) for the pG140 plasmid, Michael Reese (University of Texas Southwestern Medical Center) for the pUPRT-HA plasmid, David Sibley (Washington University) for the CRISPR/Cas9 plasmid and Caia Dominicus (Francis Crick Institute) for critically reading the manuscript. We also thank the following members of science technology platforms at the Francis Crick Institute for their support: Matt Renshaw (light microscopy), Michael Howell (high throughput screening), Damian Carragher, Rhys Hefin, Phil Hobson and Graham Preece (flow cytometry). This work was supported by awards to MT by The Francis Crick Institute (<https://www.crick.ac.uk/>), which receives its core funding from Cancer Research UK (FC001189; <https://www.cancerresearchuk.org>), the UK Medical Research Council (FC001189; <https://www.mrc.ac.uk/>) and the Wellcome Trust (FC001189; <https://wellcome.ac.uk/>). This work was supported by US Public Health Service grants AI137767 and AI139201 to GEW and National Institutes of Health grant awarded to Aoife Heaslip (AI121885).

## Competing interests

The authors have declared that no competing interests exist.

## References

Andenmatten, N., Egarter, S., Jackson, A. J., Jullien, N., Herman, J.-P., & Meissner, M. (2013).

Conditional genome engineering in *Toxoplasma gondii* uncovers alternative invasion

mechanisms. *Nature Methods*, 10(2), 125–127. doi:10.1038/nmeth.2301

Bannister, L. H., & Mitchell, G. H. (1995). The role of the cytoskeleton in *Plasmodium*

*falciparum* merozoite biology: an electron-microscopic view. *Annals of Tropical*

*Medicine and Parasitology*, 89(2), 105–111. doi:10.1080/00034983.1995.11812940

Baum, J., Papenfuss, A. T., Baum, B., Speed, T. P., & Cowman, A. F. (2006). Regulation of

apicomplexan actin-based motility. *Nature Reviews Microbiology*, 4(8), 621–628.

doi:10.1038/nrmicro1465

- 1135 Bertling, E., Hotulainen, P., Mattila, P. K., Matilainen, T., Salminen, M., & Lappalainen, P.  
1136 (2004). Cyclase-associated protein 1 (CAP1) promotes cofilin-induced actin dynamics  
1137 in mammalian nonmuscle cells. *Molecular Biology of the Cell*, 15(5), 2324–2334.  
1138 doi:10.1091/mbc.e04-01-0048
- 1139 Black, M. W., Arrizabalaga, G., & Boothroyd, J. C. (2000). Ionophore-resistant mutants of  
1140 *Toxoplasma gondii* reveal host cell permeabilization as an early event in egress. *Mol*  
1141 *Cell Biol*, 20(24), 9399–408. doi:10.1128/MCB.20.24.9399-9408.2000
- 1142 Black, M. W., & Boothroyd, J. C. (2000). Lytic cycle of *Toxoplasma gondii*. *Microbiology and*  
1143 *Molecular Biology Reviews*, 64(3), 607–623. doi:10.1128/MMBR.64.3.607-623.2000
- 1144 Brown, K. M., Long, S., & Sibley, L. D. (2017). Plasma membrane association by N-acylation  
1145 governs PKG function in *Toxoplasma gondii*. *MBio*, 8(3), e00375–17.
- 1146 Caffaro, C. E., Koshy, A. A., Liu, L., Zeiner, G. M., Hirschberg, C. B., & Boothroyd, J. C. (2013).  
1147 A nucleotide sugar transporter involved in glycosylation of the *Toxoplasma* tissue cyst  
1148 wall is required for efficient persistence of bradyzoites. *PLOS Pathogens*, 9(5),  
1149 e1003331. doi:10.1371/journal.ppat.1003331
- 1150 Deerinck, T. J., Bushong, E. A., Thor, A., & Ellisman, M. H. (2010). NCMIR methods for 3D EM:  
1151 A new protocol for preparation of biological specimens for serial block face scanning  
1152 electron microscopy. Retrieved November 21, 2018, from  
1153 [http://gatan.actonservice.com/acton/attachment/11413/f-017e/1/-/-/-/-/](http://gatan.actonservice.com/acton/attachment/11413/f-017e/1/-/-/-/-/sbfsem%20sample%20prep%20protocol.pdf?modal=1)  
1154 [/sbfsem%20sample%20prep%20protocol.pdf?modal=1](http://gatan.actonservice.com/acton/attachment/11413/f-017e/1/-/-/-/-/sbfsem%20sample%20prep%20protocol.pdf?modal=1)
- 1155 Delbac, F., Sanger, A., Neuhaus, E. M., Stratmann, R., Ajioka, J. W., Toursel, C., Herm-Gotz,  
1156 A., Tomavo, S., Soldati, T., & Soldati, D. (2001). *Toxoplasma gondii* myosins B/C: one  
1157 gene, two tails, two localizations, and a role in parasite division. *The Journal of Cell*  
1158 *Biology*, 155(4), 613–624. doi:10.1083/jcb.200012116

1159 Dobrowolski, J. M., Niesman, I. R., & Sibley, L. D. (1997). Actin in the parasite *Toxoplasma*  
1160 *gondii* is encoded by a single copy gene, ACT1 and exists primarily in a globular form.  
1161 *Cell Motility*, 37(3), 253–262. doi:10.1002/(SICI)1097-0169(1997)37:3<253::AID-  
1162 CM7>3.0.CO;2-7

1163 Egarter, S., Andenmatten, N., Jackson, A. J., Whitelaw, J. A., Pall, G., Black, J. A., Ferguson, D.  
1164 J. P., Tardieux, I., Mogilner, A., & Meissner, M. (2014). The *Toxoplasma* acto-MyoA  
1165 motor complex is important but not essential for gliding motility and host cell  
1166 invasion. *PLoS ONE*, 9(3), e91819. doi:10.1371/journal.pone.0091819

1167 Foe, I. T., Child, M. A., Majmudar, J. D., Krishnamurthy, S., van der Linden, W. A., Ward, G. E.,  
1168 Martin, B. R., & Bogyo, M. (2015). Global analysis of palmitoylated proteins in  
1169 *Toxoplasma gondii*. *Cell Host & Microbe*, 18(4), 501–511.  
1170 doi:10.1016/j.chom.2015.09.006

1171 Foe, I. T., Onguka, O., Amberg-Johnson, K., Garner, R. M., Amara, N., Beatty, W., Yeh, E., &  
1172 Bogyo, M. (2018). The *Toxoplasma gondii* active serine hydrolase 4 regulates parasite  
1173 division and intravacuolar parasite architecture. *MSphere*, 3(5), e00393-18.  
1174 doi:10.1128/mSphere.00393-18

1175 Fox, B. A., Ristuccia, J. G., Gigley, J. P., & Bzik, D. J. (2009). Efficient gene replacements in  
1176 *Toxoplasma gondii* strains deficient for nonhomologous end joining. *Eukaryotic Cell*,  
1177 8(4), 520–529. doi:10.1128/EC.00357-08

1178 Frénal, K., Dubremetz, J.-F., Lebrun, M., & Soldati-Favre, D. (2017). Gliding motility powers  
1179 invasion and egress in Apicomplexa. *Nature Reviews Microbiology*, 15, 645.  
1180 doi:10.1038/nrmicro.2017.86

1181 Frénal, K., Jacot, D., Hammoudi, P.-M., Graindorge, A., Maco, B., & Soldati-Favre, D. (2017).  
1182 Myosin-dependent cell-cell communication controls synchronicity of division in acute

1183 and chronic stages of *Toxoplasma gondii*. *Nature Communications*, 8, ncomms15710.  
1184 doi:10.1038/ncomms15710

1185 Garrison, E., Treeck, M., Ehret, E., Butz, H., Garbuz, T., Oswald, B. P., Settles, M., Boothroyd,  
1186 J., & Arrizabalaga, G. (2012). A forward genetic screen reveals that calcium-  
1187 dependent protein kinase 3 regulates egress in *Toxoplasma*. *PLoS Pathog*, 8(11).  
1188 doi:10.1371/journal.ppat.1003049

1189 Gibson, D. G., Smith, H. O., Iii, C. A. H., Venter, J. C., & Merryman, C. (2010). Chemical  
1190 synthesis of the mouse mitochondrial genome. *Nature Methods*, 7(11), 901–903.  
1191 doi:10.1038/nmeth.1515

1192 Graindorge, A., Fréchal, K., Jacot, D., Salamun, J., Marq, J. B., & Soldati-Favre, D. (2016). The  
1193 conoid associated motor MyoH is indispensable for *Toxoplasma gondii* entry and exit  
1194 from host cells. *PLoS Pathog*, 12(1), e1005388. doi:10.1371/journal.ppat.1005388

1195 Haase, S., Zimmermann, D., Olshina, M. A., Wilkinson, M., Fisher, F., Tan, Y. H., Stewart, R. J.,  
1196 Tonkin, C. J., Wong, W., Kovar, D. R., & others. (2015). Disassembly activity of actin-  
1197 depolymerizing factor (ADF) is associated with distinct cellular processes in  
1198 apicomplexan parasites. *Molecular Biology of the Cell*, 26(17), 3001–3012.  
1199 doi:10.1091/mbc.E14-10-1427

1200 Hakimi, M.-A., Olias, P., & Sibley, L. D. (2017). *Toxoplasma* effectors targeting host signaling  
1201 and transcription. *Clinical Microbiology Reviews*, 30(3), 615–645.  
1202 doi:10.1128/CMR.00005-17

1203 Halonen, S. K., & Weiss, L. M. (2013). Chapter 8 - Toxoplasmosis. In H. H. Garcia, H. B.  
1204 Tanowitz, & O. H. Del Brutto (Eds.), *Handbook of Clinical Neurology* (Vol. 114, pp.  
1205 125–145). Elsevier. doi:10.1016/B978-0-444-53490-3.00008-X



1206 Heaslip, A. T., Nelson, S. R., & Warshaw, D. M. (2016). Dense granule trafficking in  
1207 *Toxoplasma gondii* requires a unique class 27 myosin and actin filaments. *Molecular*  
1208 *Biology of the Cell*, 27(13), 2080–2089. doi:10.1091/mbc.E15-12-0824

1209 Hliscs, M., Sattler, J. M., Tempel, W., Artz, J. D., Dong, A., Hui, R., Matuschewski, K., &  
1210 Schuler, H. (2010). Structure and function of a G-actin sequestering protein with a  
1211 vital role in malaria oocyst development inside the mosquito vector. *Journal of*  
1212 *Biological Chemistry*, 285(15), 11572–11583. doi:10.1074/jbc.M109.054916

1213 Howard, B. L., Harvey, K. L., Stewart, R. J., Azevedo, M. F., Crabb, B. S., Jennings, I. G.,  
1214 Sanders, P. R., Manallack, D. T., Thompson, P. E., Tonkin, C. J., & Gilson, P. R. (2015).  
1215 Identification of potent phosphodiesterase inhibitors that demonstrate cyclic  
1216 nucleotide-dependent functions in apicomplexan parasites. *ACS Chemical Biology*,  
1217 10(4), 1145–1154. doi:10.1021/cb501004q

1218 Huynh, M.-H., & Carruthers, V. B. (2009). Tagging of endogenous genes in a *Toxoplasma*  
1219 *gondii* strain lacking Ku80. *Eukaryotic Cell*, 8(4), 530–539. doi:10.1128/EC.00358-08

1220 Jacot, D., Daher, W., & Soldati-Favre, D. (2013). *Toxoplasma gondii* myosin F, an essential  
1221 motor for centrosomes positioning and apicoplast inheritance. *The EMBO Journal*,  
1222 32(12), 1702–1716. doi:10.1038/emboj.2013.113

1223 Kim, J. H., Lee, S.-R., Li, L.-H., Park, H.-J., Park, J.-H., Lee, K. Y., Kim, M.-K., Shin, B. A., & Choi,  
1224 S.-Y. (2011). High cleavage efficiency of a 2A peptide derived from porcine  
1225 teschovirus-1 in human cell lines, zebrafish and mice. *PLOS ONE*, 6(4), e18556.  
1226 doi:10.1371/journal.pone.0018556

1227 Kozak, M. (1987a). An analysis of 5'-noncoding sequences from 699 vertebrate messenger  
1228 RNAs. *Nucleic Acids Research*, 15(20), 8125–8148. doi:10.1093/nar/15.20.8125

1229 Kozak, M. (1987b). At least six nucleotides preceding the AUG initiator codon enhance  
1230 translation in mammalian cells. *Journal of Molecular Biology*, 196(4), 947–950.  
1231 doi:10.1016/0022-2836(87)90418-9

1232 Kremer, J. R., Mastronarde, D. N., & McIntosh, J. R. (1996). Computer visualization of three-  
1233 dimensional image data using IMOD. *Journal of Structural Biology*, 116(1), 71–76.  
1234 doi:10.1006/jsbi.1996.0013

1235 Leung, J. M., Rould, M. A., Konradt, C., Hunter, C. A., & Ward, G. E. (2014). Disruption of  
1236 *TgPHIL1* alters specific parameters of *Toxoplasma gondii* motility measured in a  
1237 quantitative, three-dimensional live motility assay. *PLoS ONE*, 9(1), e85763.  
1238 doi:10.1371/journal.pone.0085763

1239 Lorestani, A., Ivey, F. D., Thirugnanam, S., Busby, M. A., Marth, G. T., Cheeseman, I. M., &  
1240 Gubbels, M. J. (2012). Targeted proteomic dissection of *Toxoplasma* cytoskeleton  
1241 sub-compartments using MORN1. *Cytoskeleton*, 69(12), 1069–85.  
1242 doi:10.1002/cm.21077

1243 Lourido, S., Tang, K., & Sibley, L. D. (2012). Distinct signalling pathways control *Toxoplasma*  
1244 egress and host-cell invasion. *The EMBO Journal*, 31(24), 4524–4534.  
1245 doi:10.1038/emboj.2012.299

1246 Magno, R. C., Lemgruber, L., Vommario, R. C., De Souza, W., & Attias, M. (2005).  
1247 Intravacuolar network may act as a mechanical support for *Toxoplasma gondii* inside  
1248 the parasitophorous vacuole. *Microscopy Research and Technique*, 67(1), 45–52.  
1249 doi:10.1002/jemt.20182

1250 Makkonen, M., Bertling, E., Chebotareva, N. A., Baum, J., & Lappalainen, P. (2013).  
1251 Mammalian and malaria parasite cyclase-associated proteins catalyze nucleotide

1252 exchange on G-actin through a conserved mechanism. *Journal of Biological*  
1253 *Chemistry*, 288(2), 984–994. doi:10.1074/jbc.M112.435719

1254 Mattila, P. K., Quintero-Monzon, O., Kugler, J., Moseley, J. B., Almo, S. C., Lappalainen, P., &  
1255 Goode, B. L. (2004). A high-affinity interaction with ADP-actin monomers underlies  
1256 the mechanism and in vivo function of Srv2/cyclase-associated protein. *Molecular*  
1257 *Biology of the Cell*, 15(11), 5158–5171. doi:10.1091/mbc.e04-06-0444

1258 McCoy, J. M., Whitehead, L., van Dooren, G. G., & Tonkin, C. J. (2012). TgCDPK3 regulates  
1259 calcium-dependent egress of *Toxoplasma gondii* from host cells. *PLoS Pathogens*,  
1260 8(12), e1003066. doi:10.1371/journal.ppat.1003066

1261 Mehta, S., & Sibley, L. D. (2011). Actin depolymerizing factor controls actin turnover and  
1262 gliding motility in *Toxoplasma gondii*. *Molecular Biology of the Cell*, 22(8), 1290–  
1263 1299. doi:10.1091/mbc.e10-12-0939

1264 Muñoz-Hernández, S., González del Carmen, M., Mondragón, M., Mercier, C., Cesbron, M. F.,  
1265 Mondragón-González, S. L., González, S., & Mondragón, R. (2011). Contribution of the  
1266 residual body in the spatial organization of *Toxoplasma gondii* tachyzoites within the  
1267 parasitophorous vacuole. *BioMed Research International*. doi:10.1155/2011/473983

1268 Nakagawa, S., Niimura, Y., Gojobori, T., Tanaka, H., & Miura, K. (2008). Diversity of preferred  
1269 nucleotide sequences around the translation initiation codon in eukaryote genomes.  
1270 *Nucleic Acids Research*, 36(3), 861–871. doi:10.1093/nar/gkm1102

1271 Ono, S. (2013). The role of cyclase-associated protein in regulating actin filament dynamics -  
1272 more than a monomer-sequestration factor. *J Cell Sci*, 126(15), 3249–3258.  
1273 doi:10.1242/jcs.128231

1274 Peng, D., & Tarleton, R. (2015). EuPaGDT: a web tool tailored to design CRISPR guide RNAs  
1275 for eukaryotic pathogens. *Microbial Genomics*, 1(4). doi:10.1099/mgen.0.000033

1276 Periz, J., Whitelaw, J., Harding, C., Gras, S., Minina, M. I. D. R., Latorre-Barragan, F.,  
1277 Lemgruber, L., Reimer, M. A., Insall, R., Heaslip, A., & Meissner, M. (2017).  
1278 *Toxoplasma gondii* F-actin forms an extensive filamentous network required for  
1279 material exchange and parasite maturation. *ELife*, 6, e24119.  
1280 doi:10.7554/eLife.24119

1281 Plattner, F., Yarovsky, F., Romero, S., Didry, D., Carlier, M.-F., Sher, A., & Soldati-Favre, D.  
1282 (2008). *Toxoplasma* profilin is essential for host cell invasion and TLR11-dependent  
1283 induction of an interleukin-12 response. *Cell Host & Microbe*, 3(2), 77–87.  
1284 doi:10.1016/j.chom.2008.01.001

1285 Pospich, S., Kumpula, E.-P., Ecken, J. von der, Vahokoski, J., Kursula, I., & Raunser, S. (2017).  
1286 Near-atomic structure of jasplakinolide-stabilized malaria parasite F-actin reveals the  
1287 structural basis of filament instability. *Proceedings of the National Academy of*  
1288 *Sciences*, 114(40), 201707506. doi:10.1073/pnas.1707506114

1289 Puhka, M., Joensuu, M., Vihinen, H., Belevich, I., & Jokitalo, E. (2012). Progressive sheet-to-  
1290 tubule transformation is a general mechanism for endoplasmic reticulum partitioning  
1291 in dividing mammalian cells. *Molecular Biology of the Cell*, 23(13), 2424–2432.  
1292 doi:10.1091/mbc.E10-12-0950

1293 Reese, M. L., Zeiner, G. M., Saeij, J. P. J., Boothroyd, J. C., & Boyle, J. P. (2011). Polymorphic  
1294 family of injected pseudokinases is paramount in *Toxoplasma* virulence. *Proceedings*  
1295 *of the National Academy of Sciences of the United States of America*, 108(23), 9625–  
1296 9630. doi:10.1073/pnas.1015980108

1297 Rommereim, L. M., Bellini, V., Fox, B. A., Pètre, G., Rak, C., Touquet, B., Aldebert, D.,  
1298 Dubremetz, J.-F., Cesbron-Delauw, M.-F., Mercier, C., & Bzik, D. J. (2016). Phenotypes



1299 associated with knockouts of eight dense granule gene loci (GRA2-9) in virulent  
1300 *Toxoplasma gondii*. *PLOS ONE*, 11(7), e0159306. doi:10.1371/journal.pone.0159306  
1301 Sahoo, N., Beatty, W., Heuser, J., Sept, D., & Sibley, L. D. (2006). Unusual kinetic and  
1302 structural properties control rapid assembly and turnover of actin in the parasite  
1303 *Toxoplasma gondii*. *Mol Biol Cell*, 17(2), 895–906. doi:10.1091/mbc.E05-06-0512  
1304 Salamun, J., Kallio, J. P., Daher, W., Soldati-Favre, D., & Kursula, I. (2014). Structure of  
1305 *Toxoplasma gondii* coronin, an actin-binding protein that relocates to the posterior  
1306 pole of invasive parasites and contributes to invasion and egress. *The FASEB Journal*,  
1307 28(11), 4729–4747. doi:10.1096/fj.14-252569  
1308 Sato, Y., Hliscs, M., Dunst, J., Goosmann, C., Brinkmann, V., Montagna, G. N., &  
1309 Matuschewski, K. (2016). Comparative *Plasmodium* gene overexpression reveals  
1310 distinct perturbation of sporozoite transmission by profilin. *Molecular Biology of the*  
1311 *Cell*, 27(14), 2234–2244. doi:10.1091/mbc.E15-10-0734  
1312 Schroeder, L. K., Barentine, A. E. S., Merta, H., Schweighofer, S., Zhang, Y., Baddeley, D.,  
1313 Bewersdorf, J., & Bahmanyar, S. (2019). Dynamic nanoscale morphology of the ER  
1314 surveyed by STED microscopy. *The Journal of Cell Biology*, 218(1), 83–96.  
1315 doi:10.1083/jcb.201809107  
1316 Seeber, F. (1997). Consensus sequence of translational initiation sites from *Toxoplasma*  
1317 *gondii* genes. *Parasitology Research*, 83(3), 309–311. doi:10.1007/s004360050254  
1318 Shaw, M. K., & Tilney, L. G. (1999). Induction of an acrosomal process in *Toxoplasma gondii*:  
1319 Visualization of actin filaments in a protozoan parasite. *Proceedings of the National*  
1320 *Academy of Sciences of the United States of America*, 96(16), 9095–9099.  
1321 doi:10.1073/pnas.96.16.9095

- 1322 Sheffield, H. G., & Melton, M. L. (1968). The fine structure and reproduction of *Toxoplasma*  
1323 *gondii*. *The Journal of Parasitology*, 54(2), 209–226. doi:10.2307/3276925
- 1324 Shen, B., Brown, K. M., Lee, T. D., & Sibley, L. D. (2014). Efficient gene disruption in diverse  
1325 strains of *Toxoplasma gondii* using CRISPR/CAS9. *MBio*, 5(3).  
1326 doi:10.1128/mBio.01114-14
- 1327 Silva, D. A. O., Lobato, J., Mineo, T. W. P., & Mineo, J. R. (2007). Evaluation of serological  
1328 tests for the diagnosis of *Neospora caninum* infection in dogs: Optimization of cut off  
1329 titers and inhibition studies of cross-reactivity with *Toxoplasma gondii*. *Veterinary*  
1330 *Parasitology*, 143(3), 234–244. doi:10.1016/j.vetpar.2006.08.028
- 1331 Skillman, K. M., Diraviyam, K., Khan, A., Tang, K., Sept, D., & Sibley, L. D. (2011).  
1332 Evolutionarily divergent, unstable filamentous actin is essential for gliding motility in  
1333 apicomplexan parasites. *PLoS Pathogens*, 7(10), e1002280.  
1334 doi:10.1371/journal.ppat.1002280
- 1335 Swapna, L. S., & Parkinson, J. (2017). Genomics of apicomplexan parasites. *Critical Reviews in*  
1336 *Biochemistry and Molecular Biology*, 52(3), 254–273.  
1337 doi:10.1080/10409238.2017.1290043
- 1338 Tomavo, S., Slomianny, C., Meissner, M., & Carruthers, V. B. (2013). Protein trafficking  
1339 through the endosomal system prepares intracellular parasites for a home invasion.  
1340 *PLoS Pathogens*, 9(10). doi:10.1371/journal.ppat.1003629
- 1341 Tosetti, N., Dos Santos Pacheco, N., Soldati-Favre, D., & Jacot, D. (2019). Three F-actin  
1342 assembly centers regulate organelle inheritance, cell-cell communication and motility  
1343 in *Toxoplasma gondii*. *ELife*, 8. doi:10.7554/eLife.42669
- 1344 Treeck, M., Sanders, J. L., Gaji, R. Y., LaFavers, K. A., Child, M. A., Arrizabalaga, G., Elias, J. E.,  
1345 & Boothroyd, J. C. (2014). The calcium-dependent protein kinase 3 of *Toxoplasma*

1346 influences basal calcium levels and functions beyond egress as revealed by  
 1347 quantitative phosphoproteome analysis. *PLoS Pathog*, 10(6), e1004197.  
 1348 doi:10.1371/journal.ppat.1004197

1349 Vaishnava, S., & Striepen, B. (2006). The cell biology of secondary endosymbiosis – how  
 1350 parasites build, divide and segregate the apicoplast. *Molecular Microbiology*, 61(6),  
 1351 1380–1387. doi:10.1111/j.1365-2958.2006.05343.x

1352 West, M., Zurek, N., Hoenger, A., & Voeltz, G. K. (2011). A 3D analysis of yeast ER structure  
 1353 reveals how ER domains are organized by membrane curvature. *The Journal of Cell*  
 1354 *Biology*, 193(2), 333–346. doi:10.1083/jcb.201011039

1355 Whitelaw, J. A., Latorre-Barragan, F., Gras, S., Pall, G. S., Leung, J. M., Heaslip, A., Egarter, S.,  
 1356 Andenmatten, N., Nelson, S. R., Warshaw, D. M., Ward, G. E., & Meissner, M. (2017).  
 1357 Surface attachment, promoted by the actomyosin system of *Toxoplasma gondii* is  
 1358 important for efficient gliding motility and invasion. *BMC Biology*, 15(1).  
 1359 doi:10.1186/s12915-016-0343-5

1360  
 1361  
 1362  
 1363  
 1364  
 1365  
 1366  
 1367  
 1368  
 1369  
 1370  
 1371  
 1372  
 1373  
 1374  
 1375  
 1376  
 1377  
 1378  
 1379  
 1380  
 1381

## Figure legends

### Figure 1: Alternative translational start sites lead to the generation of two different CAP isoforms.

(A) Sequence alignment of the first 57 amino acid residues of TgCAP with that of other Apicomplexa. Green shading indicates cysteines which are putative palmitoylation sites, yellow shading indicates methionines which are putative alternative translational start sites. (B) Subcellular localisation of a CAP-GFP fusion. Scale bar, 2  $\mu$ m. (C) Subcellular localisation of CAP by immunofluorescence assay (IFA) using rabbit anti-TgCAP antibodies. Scale bar, 2  $\mu$ m. (D) Western blot of CAP expression levels over the first 24 hours following host cell invasion using anti-TgCAP antibodies. Anti-*Toxoplasma* antibodies were used as a loading control. (E) Alignment of the *Toxoplasma* consensus translation initiation (Kozak) sequence (Seeber, 1997) with the translation initiation sequences of CAP's first (M1) and second (M37) putative translational start sites. Green shading indicates bases that correspond to the Kozak sequence. (F) Schematic of TgCAP with annotations for the two putative CAP isoforms and the mutation experiments performed to test their expression: Mutation of M1 to leucine (L) to produce shortCAP, and mutation of M37 to L producing longCAP. Green diamonds indicate putative palmitoylation sites. (G) IFA and (H) western blot of ectopic HA-tagged TgCAP isoforms and cysteine mutants (C6 and C8). Inclusion of a HA-tag makes the protein run more slowly than the untagged protein. Anti-*Toxoplasma* antibodies were used as a loading control in (H). Scale bar in (G), 5  $\mu$ m.

### Figure 2: A second generation RH $\Delta ku80$ DiCre\_T2A parasite strain stably expresses DiCre.

(A) Schematic of the DiCre\_T2A expression construct. The chloramphenicol resistance cassette (CAT) is flanked by T2A skip peptides. The two Cre subunits (FRB\_Cre2 and FKBP\_Cre1) are located on either side of the T2A::CAT::T2A cassette. The fusion protein is driven by the alpha-tubulin promoter with a SAG1 3' UTR. The red hexagon indicates the position of the stop-codon. (B) Flow cytometry analysis to determine excision efficiency of the RH DiCre\_T2A  $\Delta ku80$  line following 65 days of frequent extracellular stress. Excision is determined by a shift from Killer Red<sup>(+)</sup> to Killer Red<sup>(-)</sup> and YFP<sup>(+)</sup> expression. Parasites were analysed 22 h after induction with 50 nM rapamycin (RAP) for 4 h. Due to analysing 22 h after induction of excision, parasites still have residual KillerRed signal. (C) Table summarizing the excision efficiency of RAP treated RH DiCre\_T2A  $\Delta ku80$  parasites over time in the presence or absence of chloramphenicol selection. "Day" refers to the number of days in cell culture while "rep" corresponds to biological replicates.

### Figure 3: Generation of CAP conditional knockout and complementation strains

(A) Schematic of the CAP conditional knock out strategy using double homologous integration. The position of the 5' LoxP site in the CAP promoter is indicated as well as the predicted sizes of the PCR amplicons. (B) Agarose gel showing the expected PCR products for correct integration at the endogenous locus. (C) IFA 46 hr after treatment with DMSO or 50 nM rapamycin for 4 h. Scale bar, 5  $\mu$ m. (D) Western blot showing absence of CAP protein in the cloned  $\Delta$ CAP parasites using anti-TgCAP antibodies. Anti-*Toxoplasma* antibodies were used as a loading control. (E) Subcellular localisation and (F) Western blot of ectopic HA-tagged TgCAP isoforms, in the  $\Delta$ CAP background. Inclusion of a HA-tag makes the protein run more slowly than the untagged protein. IFA images have been individually contrast adjusted to aid in visualising protein localisation. Scale bar in (E), 5  $\mu$ m. Anti-*Toxoplasma* antibodies were used as a loading control in (F).

### Figure 4: CAP plays an important but not essential role during the lytic cycle in cell culture



**(A)** Overview of the flow cytometry competition assay (left). Competition assays of mCherry-expressing  $\Delta$ CAP and CAP complementation lines with non-fluorescent WT-complemented parasites (right). The ratio of mCherry<sup>(+)</sup> to mCherry<sup>(-)</sup> parasites was analysed by flow cytometry at day 0, 15 and 30. Data are represented as mean  $\pm$  s.d. (D0 and D30,  $n=6$ . D15,  $n=4$ ). Two-way ANOVA followed by a multiple comparison Sidak's test was used to compare means between time points. **(B)** 3D Matrigel-based motility assays performed in the absence of inducers of motility. Results are expressed as mean  $\pm$  s.d. ( $n=4$ ). Each data point corresponds to a single technical replicate from one of four independent biological replicates, on which significance was assessed using an unpaired  $t$ -test. **(C)** Invasion assay comparing  $\Delta$ CAP to the complemented lines. Data are represented as mean  $\pm$  s.d. ( $n=3$ ). One-way ANOVA followed by Dunnett's test was used to compare means to the  $\Delta$ CAP<sup>CAP</sup> mean. **(D)** Egress assay. Graph shows number of egressed vacuoles in response to BIPPO over time. Data are represented as mean  $\pm$  s.d. ( $n=3$ ). Two-way ANOVA followed by Dunnett's test was used to compare means to the  $\Delta$ CAP<sup>CAP</sup> mean. Stated significance is in comparison to  $\Delta$ CAP<sup>CAP</sup>. **(E)** Dense granule trafficking assay.  $\Delta$ CAP and CAP complemented lines were transiently transfected with SAG1 $\Delta$ GPI-mCherry that allows visualisation of dense granules. The length and speed of directed runs were recorded using fluorescence microscopy and analysed using ImageJ. Data are represented as mean  $\pm$  s.d. ( $n=3$ ). One-way ANOVA followed by Dunnett's test was used to compare means to the  $\Delta$ CAP<sup>CAP</sup> mean.

# **Figure 5: CAP is important for rosetting and rapid cell-cell communication**

**(A)** Representative fluorescence images of mCherry expressing  $\Delta$ CAP parasites and complemented isoforms (left). Quantification of rosetting vs. non-rosetting parasites (right). Data are represented as mean  $\pm$  s.d. ( $n=2$ ). One-way ANOVA followed by Dunnett's test was used to compare means to the  $\Delta$ CAP<sup>CAP</sup> mean. **(B-E)** FRAP experiments to measure transfer of mCherry between individual parasites in a vacuole. **(B)** Heatmaps showing the percentage change in fluorescence of individual parasites in (i) CAP complemented, (ii)  $\Delta$ CAP and (iii)  $\Delta$ gra2 parasite lines. A recovery plot and image for representative vacuoles are included. Regions of interest are numbered; the bleached parasite is "1". Numbers are allocated based on proximity to the bleached parasite. The yellow lightning bolt indicates which parasite was photobleached. Data are representative of two independent experiments. **(C, D)** Graphs quantifying the type (C) and amount (D) of recovery for all parasite lines. Data are represented as mean  $\pm$  s.d. ( $\Delta$ CAP and  $\Delta$ CAP<sup>CAP</sup>  $n=4$ , all other lines,  $n=2$ ). Statistical significance was assessed by either Chi-square test (D) or one-way ANOVA followed by Dunnett's test to compare means to the  $\Delta$ CAP<sup>CAP</sup> mean (C). **(E)** FRAP analysis of  $\Delta$ CAP parasites. The images and graphs represent sequential photobleaching and recovery measurements of individual parasites within the vacuole. The yellow lightning bolt indicates which parasite was photobleached. The white arrow identifies the parasite from which the majority of recovery was observed. All scale bars, 5  $\mu$ m.

# **Figure 6: CAP is important for daughter cell orientation, but not synchronous division**

**(A)** Parasites stained with anti-IMC 3 antibodies to visualise daughter cell orientation and division. Scale bar, 5  $\mu$ m. **(B)** Quantification of synchronicity of division in parasite vacuoles using daughter cell staining from (A) reveals no defect in the synchronicity of  $\Delta$ CAP parasites. Data are represented as mean  $\pm$  s.d. ( $n=3$ ). Significance was assessed using an unpaired two-tailed  $t$ -test. **(C)** Quantification of daughter cell orientation in parasite vacuoles reveals a significant defect in the daughter cell orientation of  $\Delta$ CAP parasites. Data are represented as mean  $\pm$  s.d. ( $n=3$ ). One-way ANOVA followed by Dunnett's test was used to compare means to the  $\Delta$ CAP<sup>CAP</sup> mean.

# **Figure 7: CAP KO parasites are still connected by a decentralised residual body**

**(A)** FRAP analysis of  $\Delta$ CAP<sup>CAP</sup> parasites. The images and graphs represent sequential photobleaching and recovery measurements of individual parasites within the vacuole. **(B) (i)**

FIB SEM of the vacuole from (A) with a 3D model highlighting the residual body (green skeleton representing how the approximate centre can be traced through to the basal poles) and parasite openings at the basal pole (orange ring). Note that the illustrated connections display the distance between the parasite's posterior ends, and do not represent tubular connections between them. Numbering of parasites is consistent with (A). (ii) Zoomed image of the residual body from (i), (iii) zoomed image of the residual body from (i) overlaid with the 3D model. (C) FRAP analysis of  $\Delta$ CAP parasites. The images and graphs represent sequential photobleaching and recovery measurements of individual parasites within the vacuole. (D) (i) FIB SEM of the vacuole from (A), numbering of parasites is consistent with (C). (ii) Zoomed image of the boxed region from (i). Green arrows indicate the residual body (left panel). A 3D model highlights the residual body (green skeleton drawn through the lumen of the connections between parasites), parasite openings at the basal pole (orange ring) (right panel). (iii) A 3D model of selected features in the vacuole from (C), highlighting the residual body (green), parasite openings at the basal pole (orange ring) and coarse segmentation of two of the parasites (yellow) (left panel). This model is shown with an orthoslice from the FIB SEM volume (right panel). (E) Zoomed images of the boxed region from (Di). Blue arrows indicate a putative ER structure (left). A 3D model highlights this putative ER (blue) and parasite openings at the basal pole (orange ring) (right). (i) View facing a Z orthoslice. (ii) View facing an X orthoslice. The yellow lightning bolt indicates which parasite was photobleached and the white arrow identifies the parasite from which recovery was observed (A,C). Scale bar, 5  $\mu$ m (A, C) or 1  $\mu$ m (B, D, E).

# **Figure 8: CAP is essential for virulence in type II but not type I parasites.**

(A) Survival rates of C57BL/6 mice infected with 25 RH  $\Delta$ CAP<sup>CAP</sup> or RH  $\Delta$ CAP parasites. (B) Survival rates of C57BL/6 mice infected with 50,000 Pru  $\Delta$ CAP parasites or with complementing CAP variants. (C) ELISA testing sera reactivity of naïve or *Toxoplasma* infected mice using *Toxoplasma* antigen. (D) Cyst burden in the brain of C57BL/6 mice 32 days post-infection with 5,000 Pru  $\Delta$ CAP parasites or with complementing CAP variants. For all experiments, five animals were infected for each strain.

## **Supplementary Figure 1. Endogenous tagging of CAP**

(A) Schematic of CAP endogenous tagging strategy. Arrowhead indicates CRISPR/CAS9 cut site. (B) IFA of the resulting HA-tagged line. Scale bar, 2  $\mu$ m.

## **Supplementary Figure 2. Excision efficiency testing of RH DiCre $\Delta$ ku80 $\Delta$ hxgprt**

Flow cytometry analysis to determine excision efficiency of the original RH DiCre  $\Delta$ ku80 $\Delta$ hxgprt line following 65 days of standard, non-stressing, culture conditions. Excision is determined by a shift from Killer Red<sup>(+)</sup> to Killer Red<sup>(-)</sup> and YFP<sup>(+)</sup> expression. Parasites were analysed 22 h after induction with 50 nM rapamycin (RAP) for 4 h. Due to analysing 22 h after induction of excision, parasites still have residual KillerRed signal.

## **Supplementary Figure 3. Excision testing of the CAP conditional knockout lines**

(A) Schematic of the CAP locus in the LoxPCAP conditional knockout lines. Rapamycin induced excision of CAP is detected by PCR3. (B) Diagnostic PCR of the CAP locus in the (i) LoxPCAP lines 5 d after treatment with either DMSO (D) or rapamycin (R). (ii) Excised clones were subsequently obtained from these rapamycin treated populations.

## **Supplementary Figure 4. CAP-HA expression in the $\Delta$ CAP<sup>CAP</sup> line**

Western blot on CAP expression levels in the  $\Delta$ CAP<sup>CAP</sup> strain over the first 24 hours following host cell invasion using anti-TgCAP antibodies. Anti-*Toxoplasma* antibodies were used as a loading control.

## **Supplementary Figure 5. Replication analysis of $\Delta$ CAP and the complemented lines.**

Data are represented as mean  $\pm$  s.d. ( $n=2$ ). One-way ANOVA followed by Dunnett's test was used to compare means to the  $\Delta\text{CAP}^{\text{CAP}}$  mean. "Other" refers to vacuoles with a non-power of 2 number of parasites.

### **Supplementary Figure 6. 3D Matrigel-based motility assays performed in the absence of inducers of motility.**

Results are expressed as mean  $\pm$  s.d. ( $n=4$ ). Each data point corresponds to a single technical replicate from one of four independent biological replicates, on which significance was assessed using an unpaired  $t$ -test.

### **Supplementary Figure 7. Scanning electron micrographs of intracellular $\Delta\text{CAP}$ and complemented lines**

Vacuole organisation is disrupted in  $\Delta\text{CAP}$  and  $\Delta\text{CAP}^{\text{longCAP}}$  parasite strains.

### **Supplementary Figure 8. Apicoplast segregation analysis**

Apicoplast segregation was not affected in the  $\Delta\text{CAP}$  line. Representative IFA images (left) and quantification of apicoplast segregation (right). Data are represented as mean  $\pm$  s.d. ( $n=3$ ). Significance was assessed using an unpaired two-tailed  $t$ -test. Scale bar, 5  $\mu\text{m}$ .

### **Supplementary Figure 9. Close up FIB SEM images of parasite connections in the $\Delta\text{CAP}$ vacuole from (Fig. 7C-E)**

The 3D model highlights the residual body (green skeleton representing how the approximate centre can be traced through to the basal poles), parasite openings at the basal pole (orange ring) and coarse segmentation of two of the parasites (yellow). Scale bars are not shown since these are oblique views – see Fig. 7 and Methods for scale information.

### **Video 1. Live egress imaging of a $\Delta\text{CAP}^{\text{CAP}}$ vacuole**

Egress was induced by addition of 50  $\mu\text{M}$  BIPPO at 0 s. Image taken every 1.8 s. The video is played at 6.6 fps and the time is indicated in seconds. Scale bar, 10  $\mu\text{m}$ .

### **Video 2. Live egress imaging of a $\Delta\text{CAP}$ vacuole**

Egress was induced by addition of 50  $\mu\text{M}$  BIPPO at 0 s. Image taken every 1.8 s. The video is played at 6.6 fps and the time is indicated in seconds. Scale bar, 10  $\mu\text{m}$ .

### **Video 3. Live egress imaging of a $\Delta\text{CAP}^{\text{shortCAP}}$ vacuole**

Egress was induced by addition of 50  $\mu\text{M}$  BIPPO at 0 s. Image taken every 1.8 s. The video is played at 6.6 fps and the time is indicated in seconds. Scale bar, 10  $\mu\text{m}$ .

### **Video 4. Live egress imaging of a $\Delta\text{CAP}^{\text{longCAP}}$ vacuole**

Egress was induced by addition of 50  $\mu\text{M}$  BIPPO at 0 s. Image taken every 1.8 s. The video is played at 6.6 fps and the time is indicated in seconds. Scale bar, 10  $\mu\text{m}$ .

### **Video 5. FRAP on a $\Delta\text{CAP}^{\text{CAP}}$ vacuole**

A single parasite was photobleached at 3 s. Images taken every 1 s. The video is played at 2 fps and the time is indicated in seconds. Scale bar, 5  $\mu\text{m}$ .

### **Video 6. FRAP on a $\Delta\text{CAP}$ vacuole**

A single parasite was photobleached at 3 s. Images taken every 1 s. The video is played at 2 fps and the time is indicated in seconds. Scale bar, 5  $\mu\text{m}$ .

### **Video 7. FRAP on a $\Delta\text{Gra2}$ vacuole**

A single parasite was photobleached at 3 s. Images taken every 1 s. The video is played at 2 fps and the time is indicated in seconds. Scale bar, 5  $\mu\text{m}$ .

**Video 8. FIB SEM of the  $\Delta$ CAP<sup>CAP</sup> vacuole from Fig. 7A-B with 3D model overlay**

All FIB SEM slices of the  $\Delta$ CAP<sup>CAP</sup> vacuole Fig. 7A-B. The 3D model highlights the residual body (green skeleton representing how the approximate centre can be traced through to the basal poles, along with a structure that extends from that centre but has no connection) and parasite openings at the basal pole (orange ring). The volume of the FIB SEM dataset shown is indicated in the Materials and methods.

**Video 9. FIB SEM of the  $\Delta$ CAP vacuole from Fig. 7C-E with 3D model overlays**

All FIB SEM slices of the  $\Delta$ CAP vacuole Fig. 7C-E. The 3D model highlights the residual body (green skeleton drawn through the approximate central axis of the lumen of the connections between parasites), parasite openings at the basal pole (orange ring), coarse segmentation of the central part of two of the parasites (yellow), and part of the putative ER (blue, note that only a selected region was segmented; from the inner face of two of the basal pores through part of the decentralised residual body). The volume of the FIB SEM dataset shown is indicated in the Materials and methods.

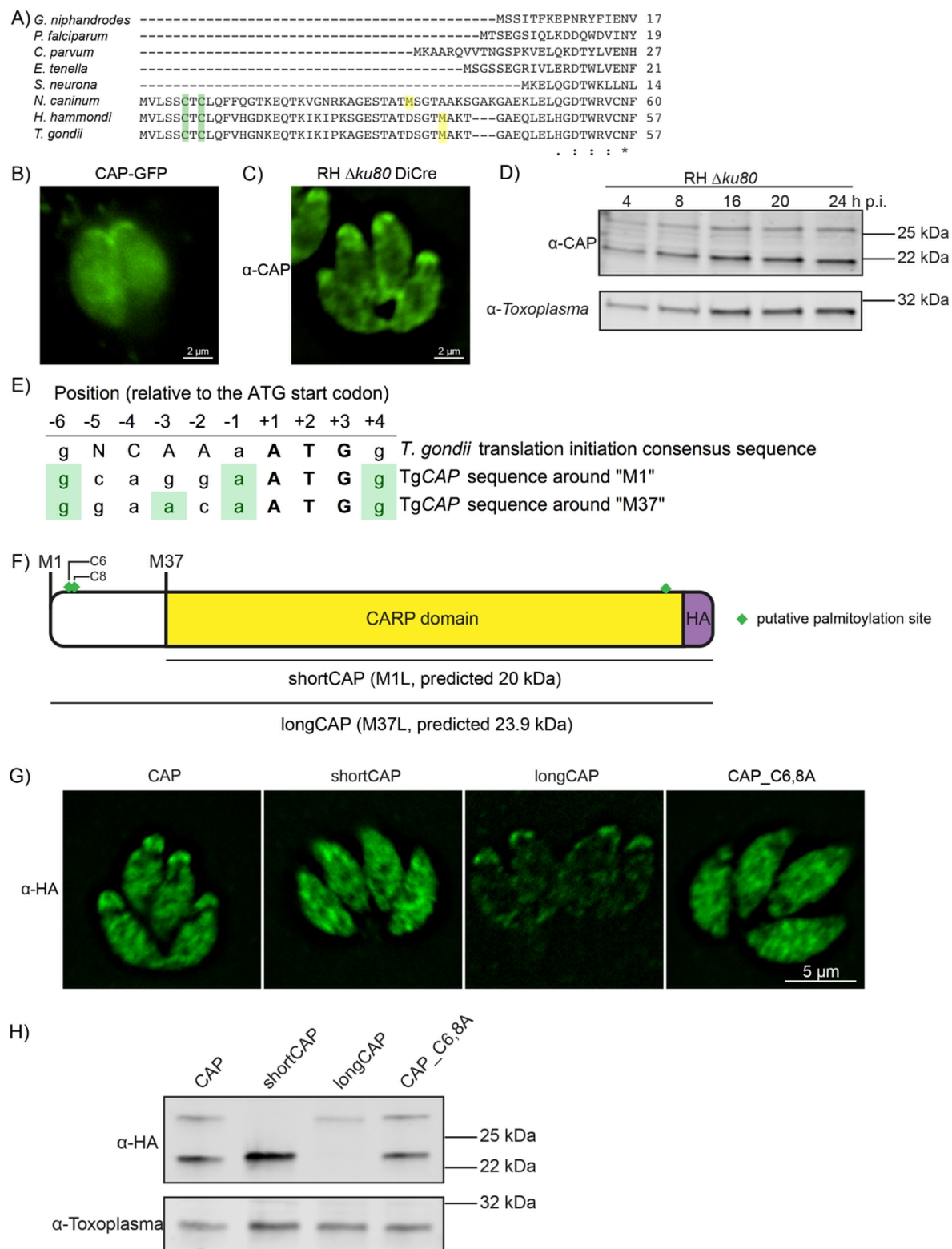
**Supplementary File 1. Primers listed in the Materials and methods**

**Supplementary File 2. Synthetic DNA listed in the Materials and methods**

**Supplementary File 3. BioWave program details for FIB SEM**



# 1618 Figure 1



1619  
1620  
1621  
1622  
1623  
1624

**Figure 2**

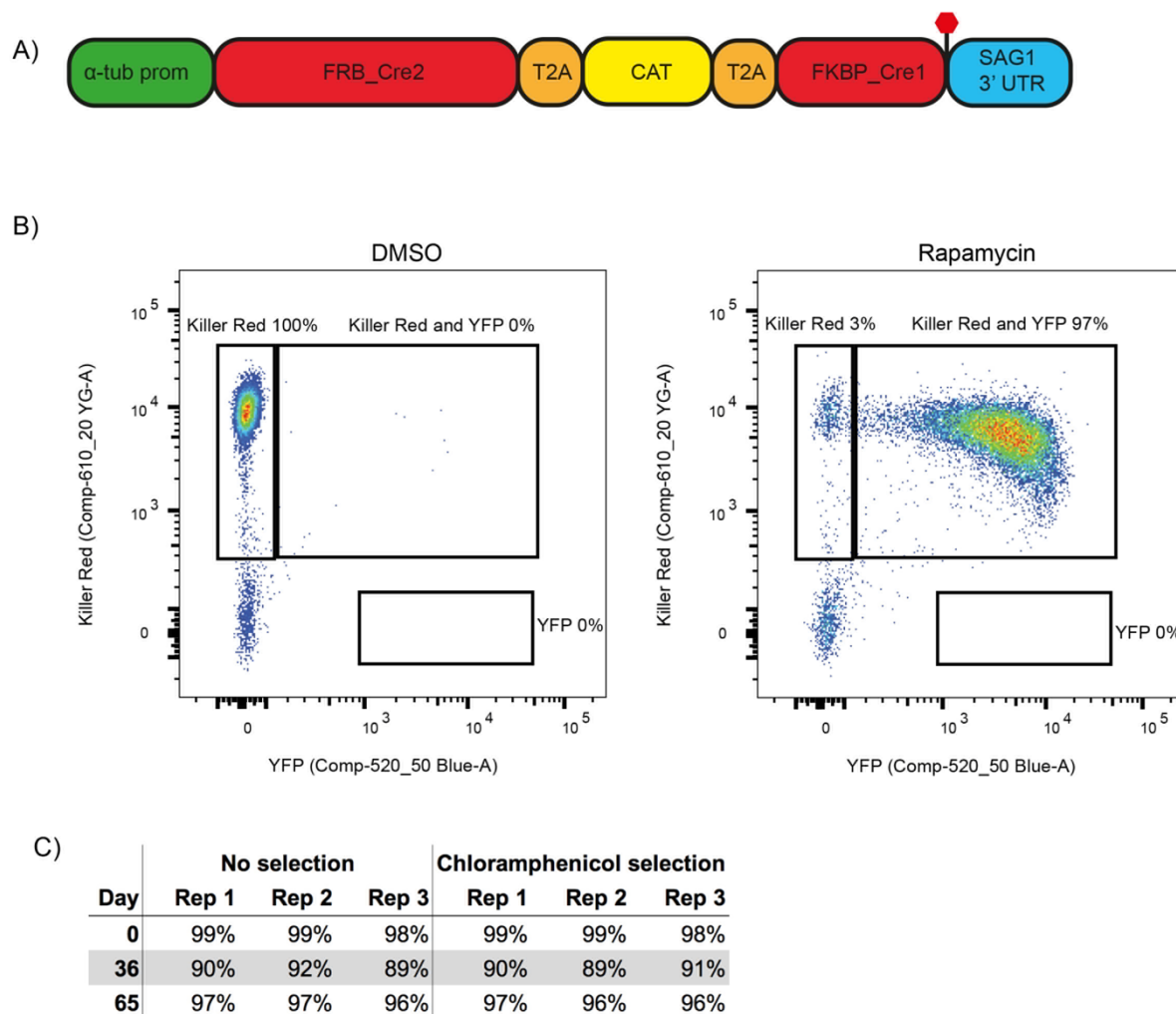


**Figure 3**

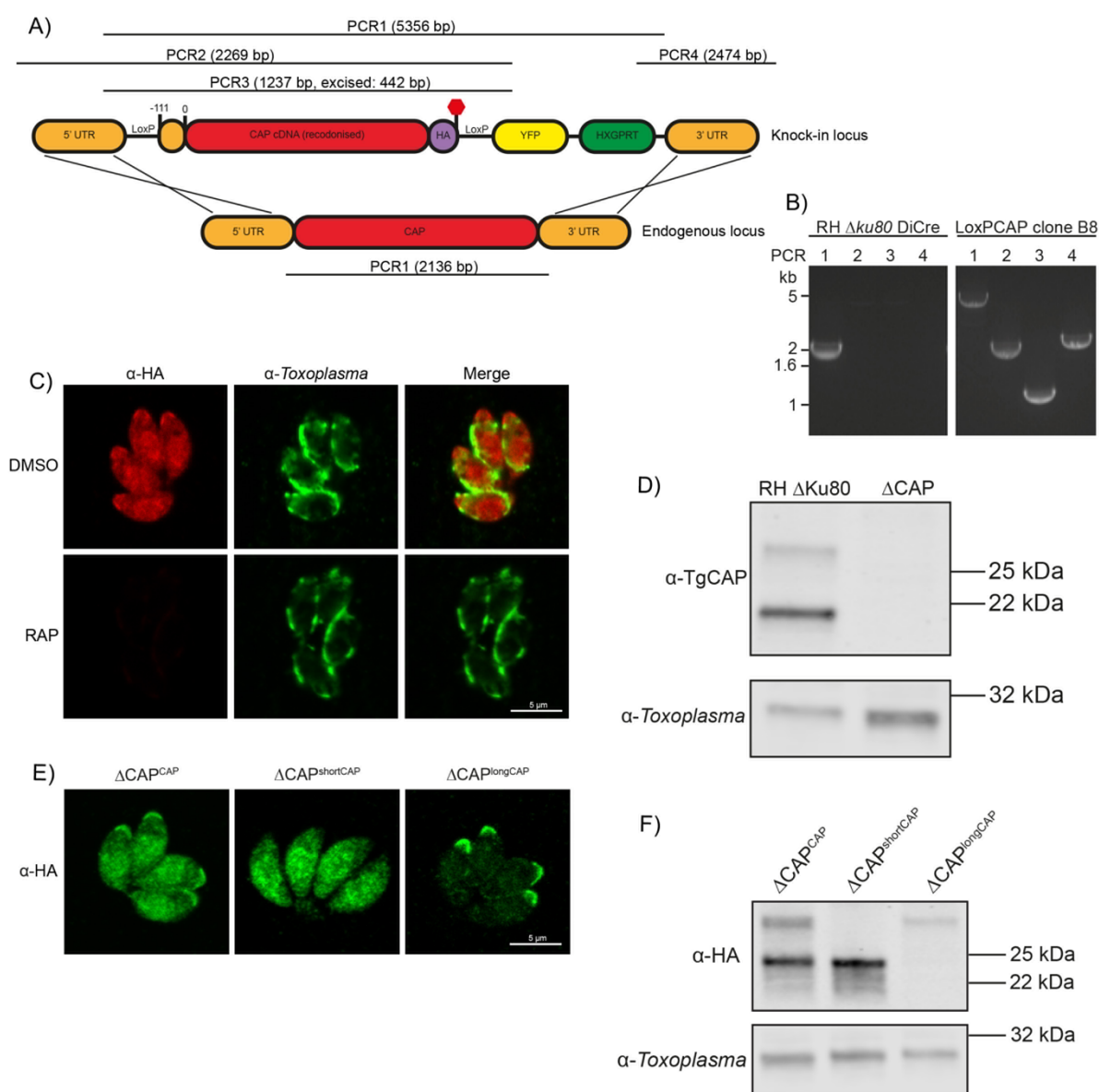
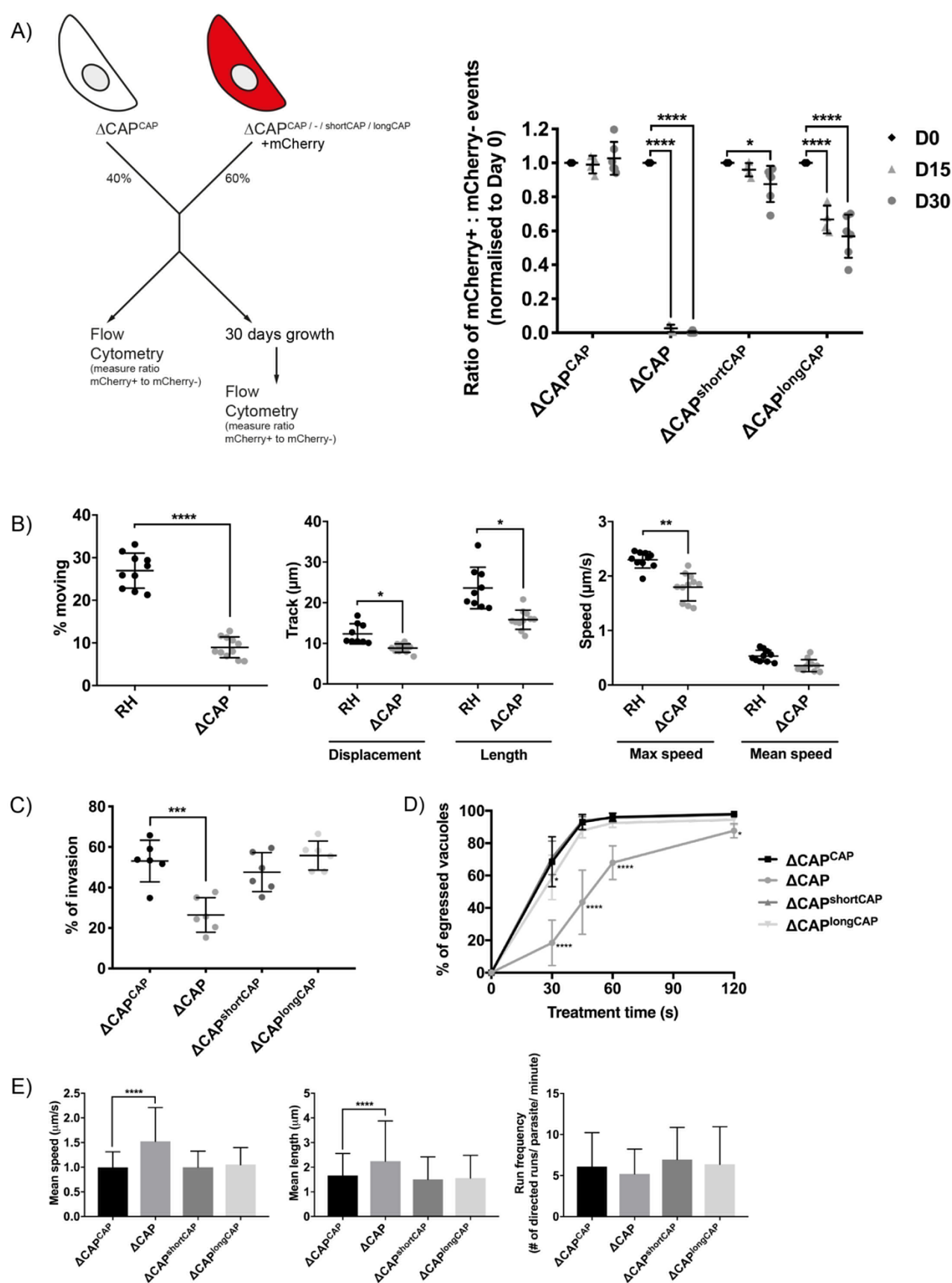


**Figure 4**





# 1674 Figure 5

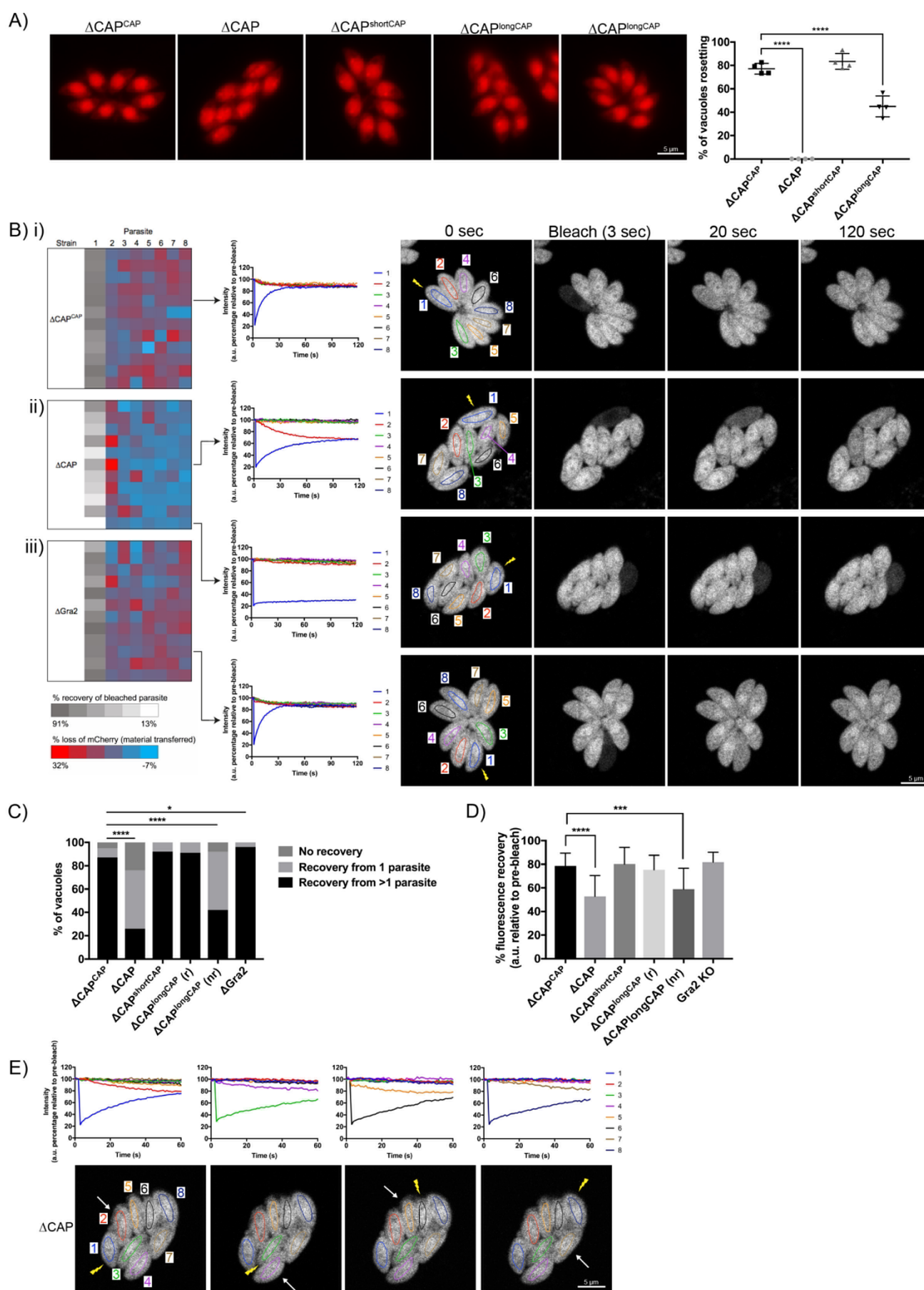
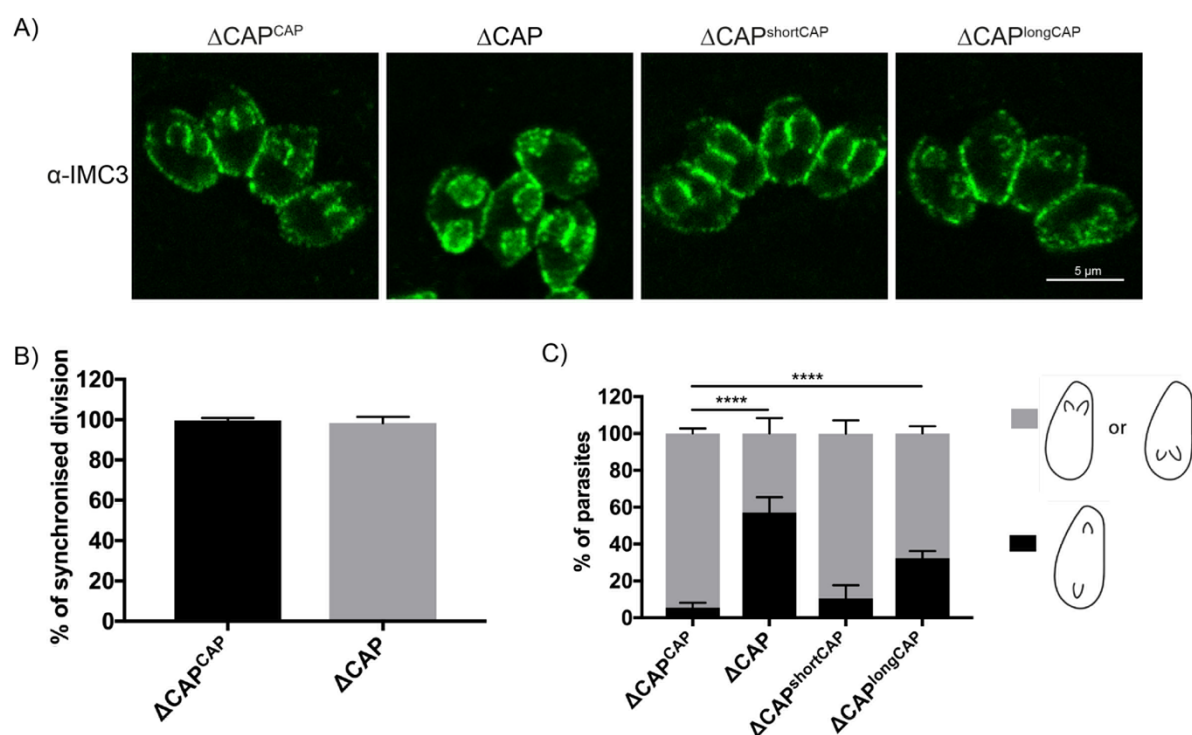
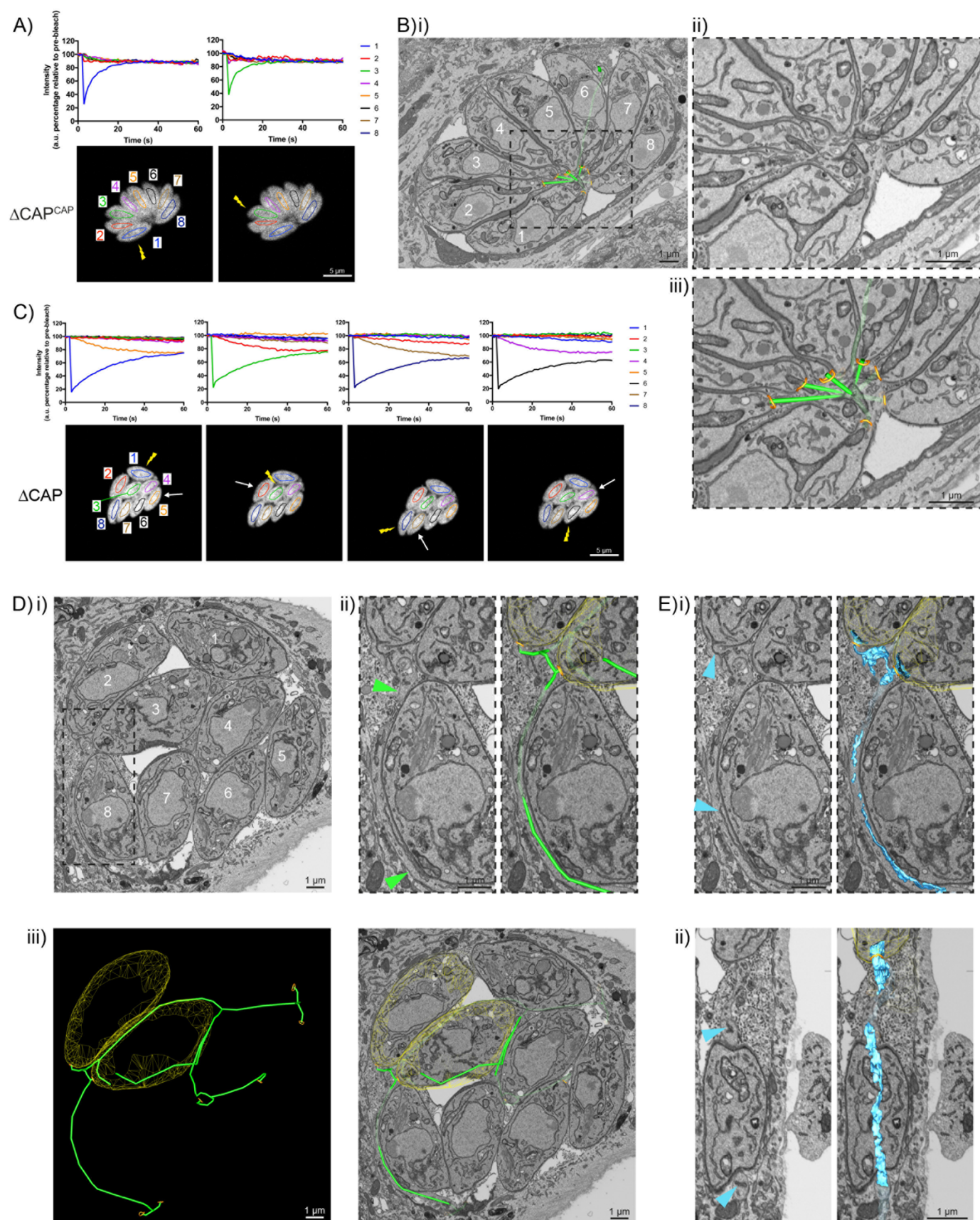


**Figure 6**



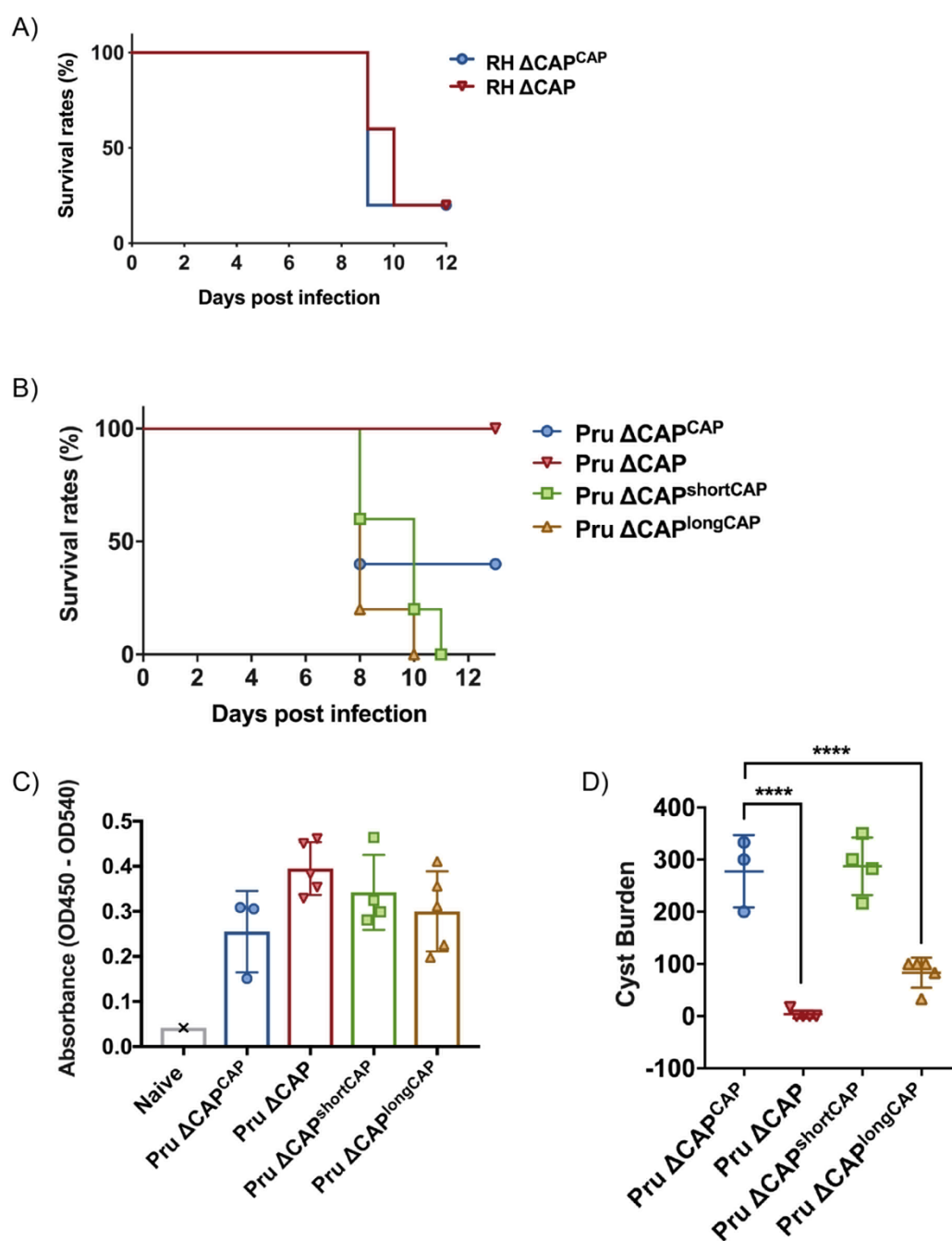
# 1707 **Figure 7**



1708  
1709

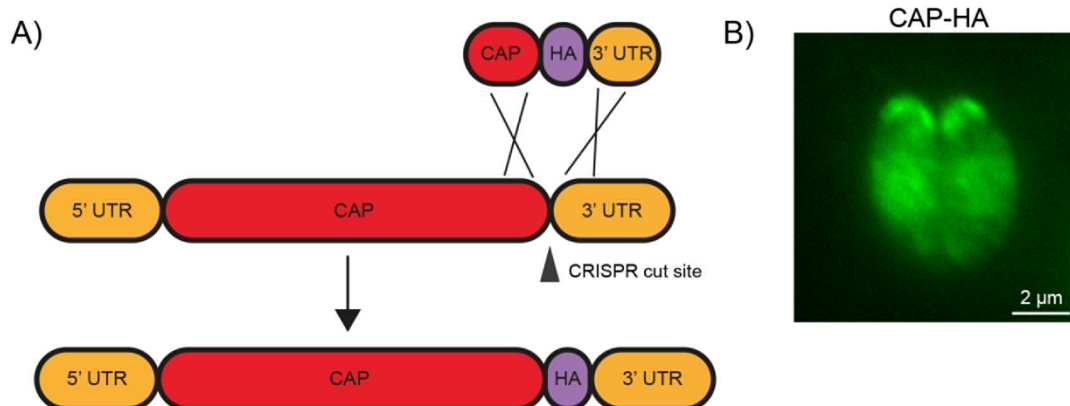


**Figure 8**

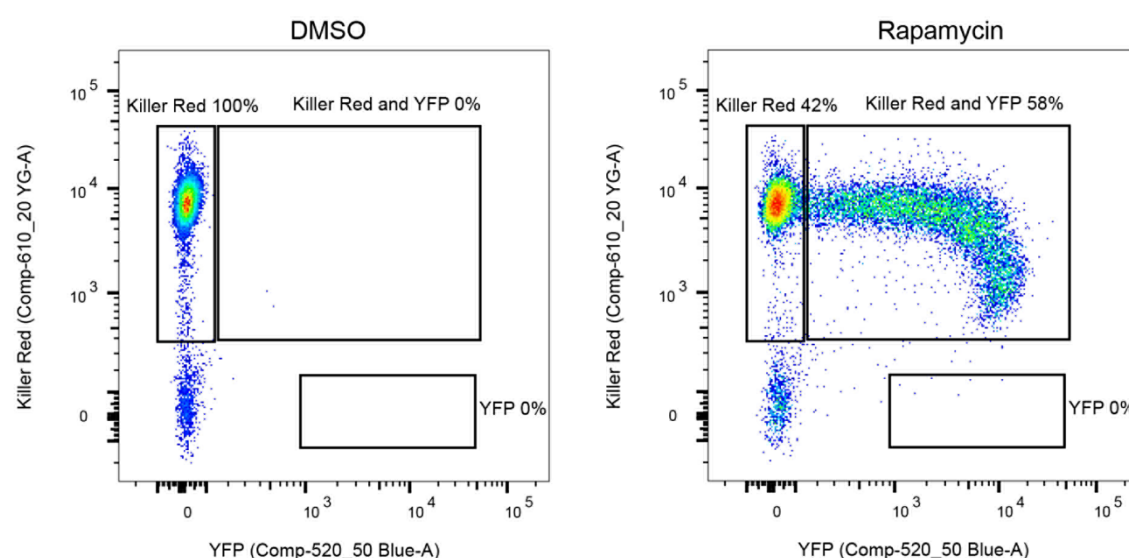




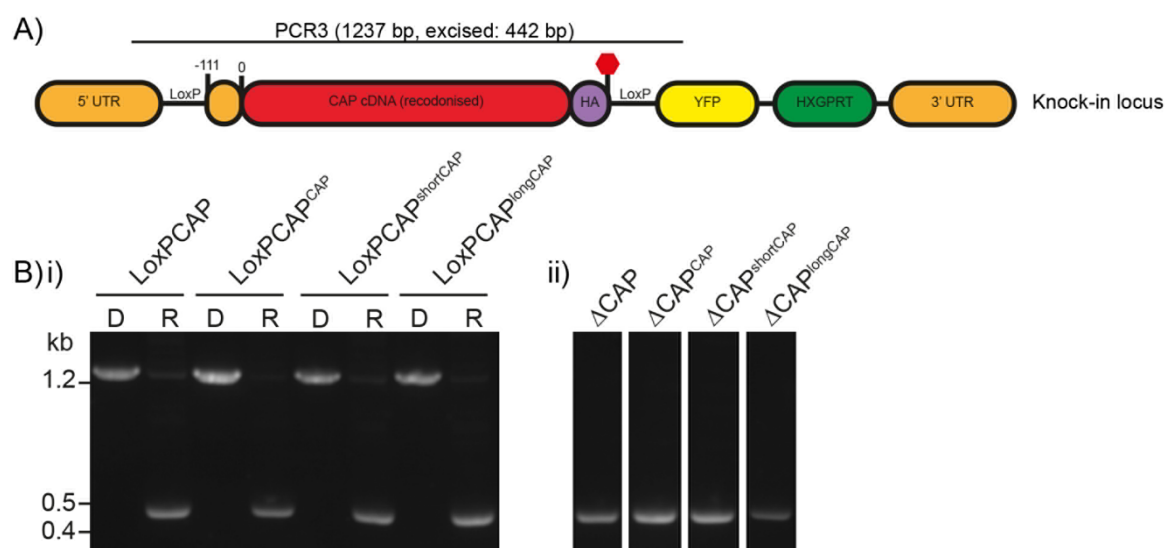
# Supplementary Figure 1



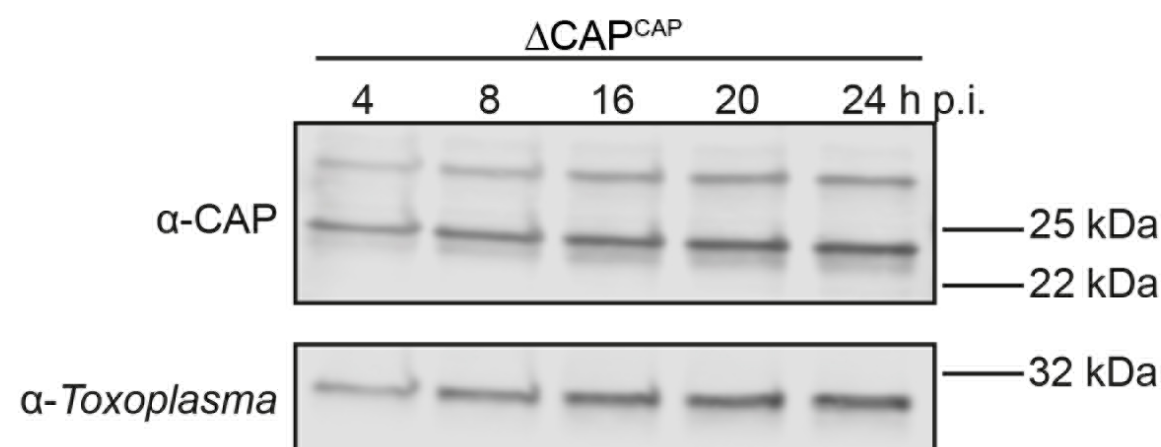
## Supplementary Figure 2



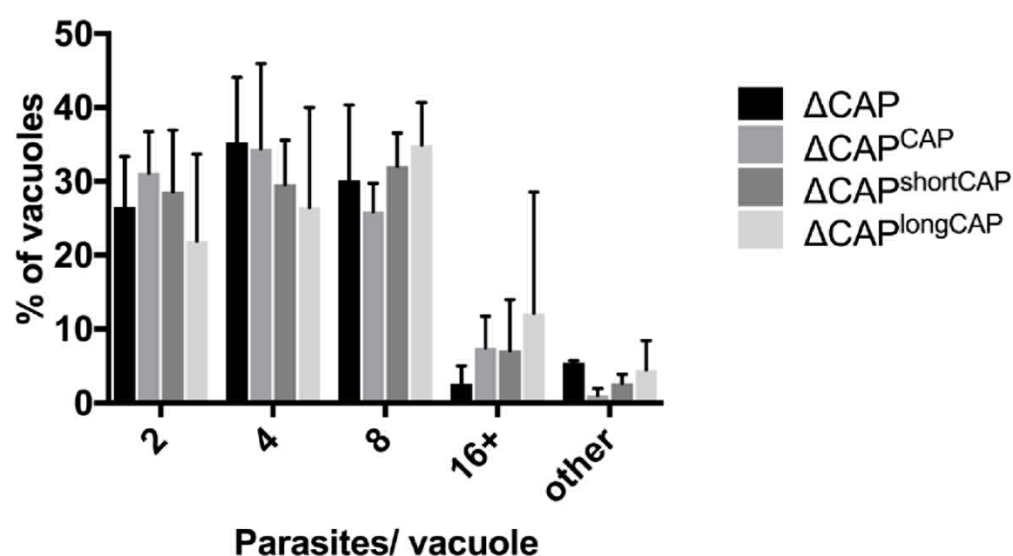
# Supplementary Figure 3



# Supplementary Figure 4

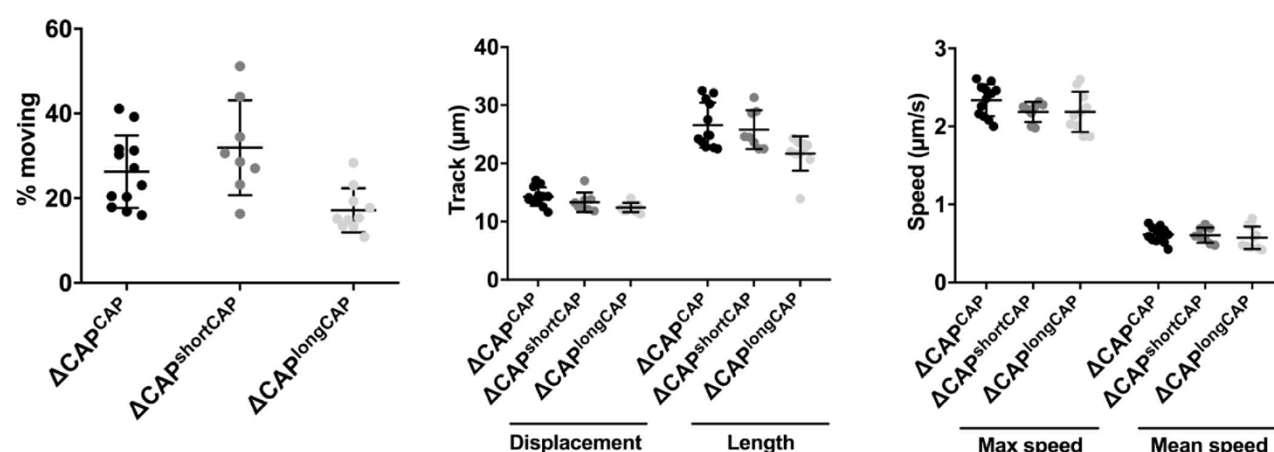


# Supplementary Figure 5

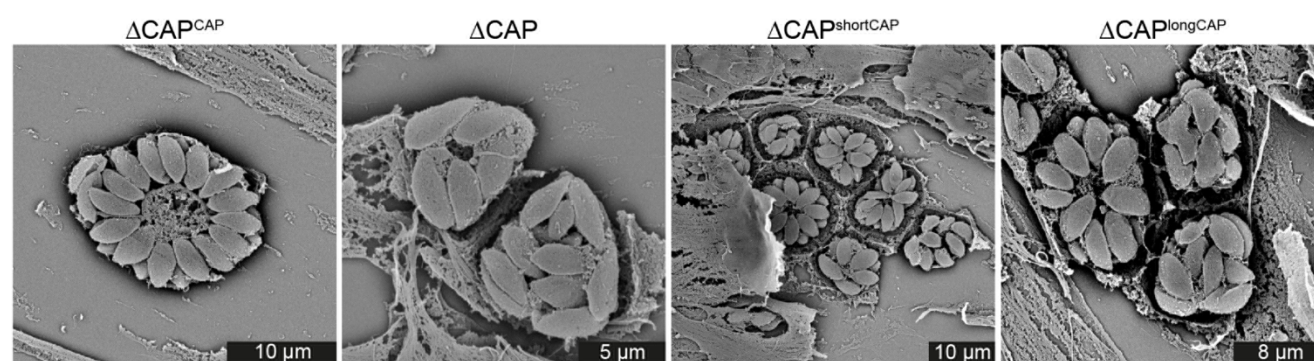




# Supplementary Figure 6

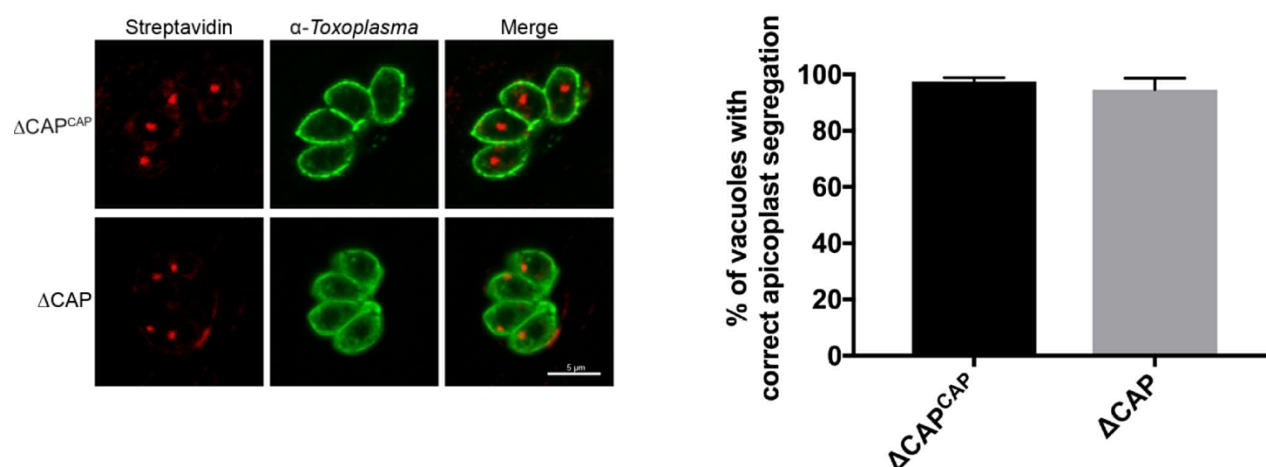


# 2002      **Supplementary Figure 7**



2003  
2004  
2005  
2006  
2007  
2008  
2009  
2010  
2011  
2012  
2013  
2014  
2015  
2016  
2017  
2018  
2019  
2020  
2021  
2022  
2023  
2024  
2025  
2026  
2027  
2028  
2029  
2030  
2031  
2032  
2033  
2034  
2035  
2036  
2037  
2038  
2039  
2040  
2041  
2042  
2043  
2044

# Supplementary Figure 8



# Supplementary Figure 9

